

RAM

● ROBOTICS
AND
MECHATRONICS

PNEUMATIC POSITION SENSING FOR ROBOTIC APPLICATIONS IN AN MR-ENVIRONMENT

M.S. (Michiel) Nikken

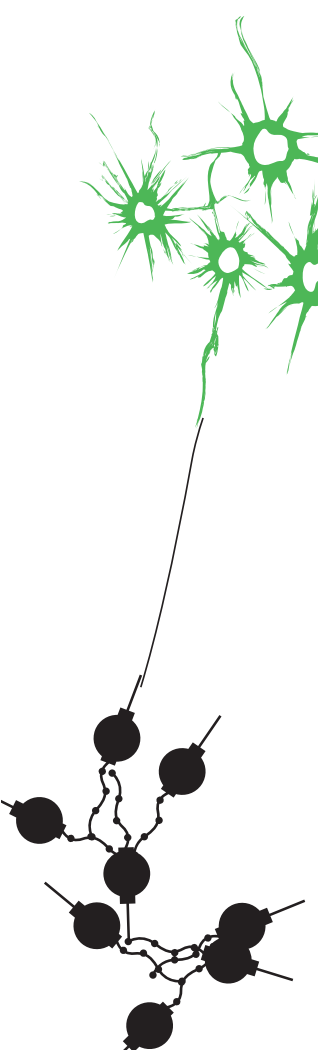
BSC ASSIGNMENT

Committee:

dr. ir. M. Abayazid
G. Wardhana, MSc
ir. E.E.G. Hekman

July, 2022

036RaM2022
Robotics and Mechatronics
EEMCS
University of Twente
P.O. Box 217
7500 AE Enschede
The Netherlands



Summary

Researchers have shown interest in developing robots that can assist in medical interventions inside an MRI-scanner. To ensure the safety of the patient and medical personnel, it is preferable that the materials in the MRI-scanner are not ferromagnetic and nonconductive, which also means that no electronics can be used. This requires an alternative approach to actuating these robots and providing them with feedback through sensors.

In order to obtain position feedback for these robots, position sensors are required. Different types of sensors have been used for this purpose, many of which use electronics inside the MRI-bore. MR Safe position sensors exist in the form of fibre optic sensors, but they are expensive.

This research explores the possibility of making an MR Safe position sensor using pneumatics. The proposed design modulates airflow through a pneumatic tube by mechanically changing the size of a constriction at the end of the tube. This creates a differential pressure across the tube, which can be measured away from the MR-environment. Using 3D printing, the pneumatic position sensor was fabricated. An iterative design approach was used to linearise and improve the sensor design.

Furthermore, a parametric analysis has been performed on two important system parameters. Next, a static characterisation of the best prototype has been carried out. An absolute mean error of 0.31 mm (0.7% of the full range) and an absolute maximum error 7.2 mm (16% of the full range) have been observed.

Additionally, to overcome some issues with the previous prototypes, like the loss of sensitivity when scaling up the sensor, a pneumatic encoder has been designed and fabricated. Tests on this encoder showed a mean error of 0.81 mm (2.0% of the tested range) and an absolute maximum error of 8.2 mm (20.5% of the tested range). Time constraints prevented multiple design iterations and a complete characterisation to be carried out. Hence, the encoder still has plenty of potential to improve the design, without requiring high-end 3D printers or similar manufacturing techniques.

Contents

Summary	iii
1 Introduction	1
1.1 MRI-guided robotics	1
1.2 Related work	1
1.3 Thesis scope	2
2 Background	4
2.1 Sensor requirements	4
2.2 Working principle	4
3 Methodology	6
3.1 Experimental setup	6
3.2 Sensor material	7
3.3 Sensor Design	8
3.4 Parametric analysis	14
3.5 Sensor Characterisation	14
4 Results and discussion	17
4.1 Sensor iteration	17
4.2 Parametric analysis	20
4.3 Sensor characterisation	23
4.4 Limitations	25
5 Pneumatic encoder	26
5.1 Sensor Design	26
5.2 Results	29
5.3 Discussion	29
6 Conclusion	32
6.1 Conclusion	32
6.2 Future work	33
A Pictures of sensor heads	34
B Multiple Regression	37
Bibliography	38

1 Introduction

The first documented application of a surgical robot dates back to 1985, when a modified UNIMATION PUMA 200 robot was used to perform a neurobiopsy under guidance of computed tomography (CT) (Kwoh et al., 1988). Since then, the field of surgical robotics has received an increasing amount of research attention due to the advantages that robotic systems have to offer. For instance, robotic systems allow for the execution of minimally invasive procedures with high accuracy and high precision. Additionally, the possibility for autonomy or semi-autonomy of surgical robotics can decrease the importance of the dexterity of the physician to the result of the intervention or biopsy (Siepel et al., 2021). Also, robotic systems can be integrated with different medical imaging modalities, such as computed tomography (CT), ultrasound (US) or magnetic resonance imaging (MRI) (Unger et al., 2021).

1.1 MRI-guided robotics

MRI is a medical imaging modality that offers high contrast imaging of soft tissue in three dimensions. Also, MRI does not expose patients or medical personnel to ionising radiation. Using robotic systems to execute these interventions under MRI guidance potentially has a lot of benefits. The stiffness of a robotic system can lead to a higher precision compared to manual intervention by a physician (Siepel et al., 2021). Additionally, in some interventions, like traditional laser ablation procedures, patients have to be moved in and out of the MRI-scanner repeatedly to confirm the position of the needle (Franco et al., 2016). Robots that operate inside the MRI-bore allow for real time guidance and can therefore reduce the procedure time.

However, the MRI scanner creates a challenging environment for robots to operate, due to strong static and dynamic magnetic fields and electromagnetic pulses. Currents are induced in conductive materials, which could be detrimental for electronics. Furthermore, these materials may distort the magnetic field which causes artifacts in the imaging, deteriorating imaging quality. Moreover, ferromagnetic materials can form a hazard due to the magnetic forces acting on it. These factors put stringent material requirements on the robots. The American Society for Testing and Materials (ASTM) has standardised the labeling of items in a magnetic resonance (MR) environment (U.S. Department of Health and Human Services, 2021, p.3). The items are categorised as follows:

1. MR Unsafe: "A medical device which poses unacceptable risks to the patient, medical staff or other persons within the MR environment."
2. MR Conditional: "A medical device with demonstrated safety in the MR environment within defined conditions including conditions for the static magnetic field, the time-varying gradient magnetic fields, and the radiofrequency fields."
3. MR Safe: "A medical device that poses no known hazards resulting from exposure to any MR environment. MR Safe medical devices are composed of materials that are electrically nonconductive, nonmetallic, and nonmagnetic."

It is important to ensure that all components of the robot in the MRI scanner are MR safe or MR conditional.

1.2 Related work

To create robotic systems with sufficient positional accuracy, it is useful to have sensors that can provide position feedback. However, conventional position sensors contain conductive materials and hence they cannot directly be implemented on robots that are to be used in MR-

environments. A number of methods have been tried in an attempt to overcome this problem and accurately control the robot's configuration.

1.2.1 Conventional position sensors

Conventional position sensors can be used if they are sufficiently shielded from MR. For instance, Navarro-Alarcon et al. (2017) and Yang et al. (2014) made robotic systems that use resistive sensors to measure the robots configuration. Even without shielding, some conventional sensors can be used. Elhawary et al. (2008) used optical encoders that were small enough to reduce the impact on image quality and minimise the safety risks. However, the signal to noise ratio is decreased up to 9.1% for some imaging sequences. Additionally, exhaustive testing needs to be done to ensure the safety of patients and personnel.

1.2.2 Fiber optic sensing

Many robotic systems intended for use inside an MRI scanner use fiber optic sensing for position feedback. Fiber optic sensing is a group of sensing techniques that is particularly attractive for use in MR-environments because of its superior MR-compatibility (Xinran et al., 2021). Sensing is achieved through manipulating light at the sensing location and redirecting it to a light sensor through optical fibers. For example, a Bragg grating can be used to filter a known incoming spectrum. Measuring the returning spectrum provides information on the strain of the Bragg grating, which can be used in force and temperature sensing (Taffoni et al., 2013). However, this method of sensing requires a costly spectral analyser.

Another method of fiber optic sensing is intensity based. A beam of light is sent through the optical fiber and the amount of light that is reflected back is modulated by the distance and type of the material at the end of the fiber. This method allows for the creation of fiber optic position encoders, like the ones that have been used in the systems developed by Gassert et al. (2006), Liu et al. (2020) or the actuator by Senturk and Patoglu (2017).

1.2.3 Feed forward and alternative methods

Some systems aim to remove the need for sensing inside the MR-environment. Groenhuis et al. (2018) control a system that is actuated using pneumatic stepper motors using feed-forward control. However, this method may fail if the stepper motors skip a step.

Alternatively, sensor systems have been used that utilise the native magnetic field of the MRI-scanner to determine the position of a magnetic field sensor. The spatial location of the sensor can be calculated using the measured magnetic field and a calibration that is carried out beforehand (Yang et al., 2014). However this method is sensitive to errors introduced by field inhomogeneities.

Of the aforementioned position sensing methods, only fibre optic sensing is unaffected by the changing magnetic fields in the scanner. However, due to the costly equipment that is required, it may be desirable to develop an alternative way of sensing.

1.3 Thesis scope

Numerous robotic systems have been proposed for use inside an MRI scanner that utilise pneumatic actuators (Navarro-Alarcon et al., 2017; Yang et al., 2014; Franco et al., 2016; Groenhuis et al., 2020). Harnessing the power of the pneumatic power source that is already available for these actuators, it may be possible to create a pneumatically based position sensor for the moving elements of such robot. Since many hospitals are equipped with pneumatic infrastructure, these robots may be cheaper to implement in the hospital routine than robots that require complex equipment, like a spectral analyser. The goal of this project is stated below and can be divided into three fundamental subquestions.

Goal To design a pneumatic position sensor for robotic applications in an MR-environment.

Subquestion 1 Which requirements does the MR-environment impose on the sensor design?

Subquestion 2 Which requirements does the robotic system impose on the sensor design?

Subquestion 3 How can translational motion be transduced into a differential pressure signal?

In this project, a position sensor will be designed and analysed. Additionally, a prototype of the design will be fabricated and its performance will be assessed.

2 Background

This pneumatic sensing project has arisen from a MSc assignment by Shametaj (2021). Shametaj designed a robot to execute percutaneous needle insertions, specifically to perform irreversible electroporation (IRE) procedures, under MRI guidance. The robot is actuated using pneumatic stepper motors. Its structure and actuators were designed to be MR-Safe. However, the position feedback system was not designed to be MR-Safe, as the robot uses a camera to provide visual position feedback. Practical reasons, like the limited amount of time and cost considerations, were the motivation for this design decision. Since the robot features pneumatic stepper motors, a pneumatic power source is already available in this system, which is convenient for the implementation of a pneumatic sensor.

Shametaj concludes that the visual feedback system that was implemented did not suffice to provide accurate feedback inside an MRI scanner and reports a tracking error between 2-6 mm and a calibration error of 1-2mm for the final trackers used in the project. In their conclusion it is suggested that the implementation of physical sensors may reduce calibration errors, improve accuracy and allow for better MRI compatibility. This project seeks to improve on these issues in a cost-effective way by using pneumatic sensing.

The robotic system uses 3D-printed linear stepper motors designed by Groenhuis et al. (2018). Three out of four joints are translational joints. In the implementation on the robot, these motors have ranges between 47.2 mm and 70.6 mm (Shametaj, 2021).

This section explains the working principle of the sensor after discussing which requirements this application sets on the position sensor.

2.1 Sensor requirements

Various requirements need to be taken into account for the design of the sensor. Some of these are related to the operation in a medical context or inside an MRI-scanner, while others are related to the ability of the sensor to enable closed-loop control of robotic systems. The requirements taken into account in this project are listed below.

- MR-Safe (or, alternatively, MR-Conditional) material
- Full stroke range
- Accuracy
- Precision

The definition of MR-Safe has been introduced in section 1 and should be adhered to. For the initial design of this project, a full stroke range of 45 mm is required. This will not suffice for most robotic applications, so the scalability of this design will be investigated. The required accuracy for a position sensor may depend on the exact medical application. Shametaj aims for application for IRE procedures but the design of a position sensor is ideally more generally applicable. According to Glossop (2012), an accuracy of 1-2 mm will suffice for most medical applications. Since in sensor applications the accuracy encapsulates the total error budget, additional specifications on the precision are not strictly required. The precision should be balanced against other sources of error to produce the desired accuracy.

2.2 Working principle

The sensor in this project is based on the principle that a pipe flow upstream can be affected by a constriction downstream. The sensor couples displacement of robotic actuators inside the

MRI-scanner to the size of an orifice at the end of a pneumatic tube and in this way it modulates the flow through the tube. This flow modulation can then be sensed upstream, away from the MRI-scanner. The sensing of the flow could be done through a flow sensor, but a cheaper alternative is to use a differential pressure sensor that measures the pressure across a section of the pneumatic tube. The pressure drop across that section of the tube is indicative for the flow.

The sensor can be modelled as follows: A compressor and regulator valve supply a potential difference against the ambient air pressure. This regulator valve then connects to the pneumatic tube. Next, this pneumatic tube connects to the device that transduces the position of the actuator to the size of an orifice that opens up the pneumatic system to ambient air. This device will from now on be referred to as 'sensor head'. The pneumatic tube and sensor head can be modelled as two series resistances, as defined according to equation 2.1, where Δp_i is the pressure across the element and Q is the air flow. The total pressure drop is then given by equation 2.2.

$$R_i = \frac{\Delta p_i}{Q} \quad (2.1)$$

$$\Delta p = \Delta p_1 + \Delta p_2 \quad (2.2)$$

Here, Δp_1 is the pressure drop from the pneumatic tube that leads up to the sensor head and Δp_2 is the pressure drop across the sensor head. The resistance of the pneumatic tube depends on the flow conditions. If the flow is laminar, it follows the Hagen-Poiseuille equation (equation 2.3), where μ is the dynamic viscosity, L the pipe length, Q the volumetric flow rate and r the (inner) tube radius. The resistance of the tube is then given by equation 2.4.

$$\Delta p_1 = \frac{8\mu L Q}{\pi r^4} = R_1 Q \quad (2.3)$$

$$R_1 = \frac{8\mu L}{\pi r^4} \quad (2.4)$$

However, if the flow is turbulent, this linear model is no longer be valid. Instead, the Darcy-Weisbach equation applies (Georgantopoulou and Georgantopoulos, 2018), as is given in equation 2.5, where f_D is the Darcy friction factor and V the mean fluid velocity. The friction factor in turn depends on the Reynolds number Re and the relative roughness of the pipe ϵ/d .

$$\Delta p_1 = \frac{f_D}{2} \cdot \frac{L}{d} \rho V^2 \quad (2.5)$$

The sensor head also poses a resistance to the air flow. This sensor head contains a narrow constriction to the ambient pressure. It is more difficult to formulate an analytical model for the resistance of this component, because the exact geometry is not yet known and viscosity, compressibility and surface roughness may all play a role when the air is pushed through a narrow space. Instead, calibration of the system will be used to characterise the relation between actuator position and voltage output of the differential pressure sensor.

3 Methodology

The final sensor design will be achieved through a prototyping process. This chapter explains the methodology that is used to perform measurements on the different prototypes and how each prototype is updated using previous measurement results. The pneumatic encoder is not included in this chapter, since it is considered an extension of the design introduced in this chapter and is therefore placed in a separate chapter (see chapter 5).

3.1 Experimental setup

It is important to use a consistent experimental setup to test different prototypes of the sensor heads. The main components of this setup are described below. A picture of the main part of the setup can be found in figure 3.1 and a schematic diagram of the measurement setup can be found in figure 3.2.

A pneumatic tube was connected between a pressure regulator and the sensor head. Using push-in fittings, pneumatic tubes were attached at the ends of this main tube such that the differential pressure sensor could measure the pressure difference across the main tube (also referred to as 'measurement tube' since this is the tube across which the differential pressure is measured). The differential pressure sensor used in this project is the MPX 5010DP (NXP, Eindhoven, Netherlands) that can measure between 0 kPa and 10 kPa and has an output between 0 V and 5 V. Its sensitivity is 450 mV/kPa.

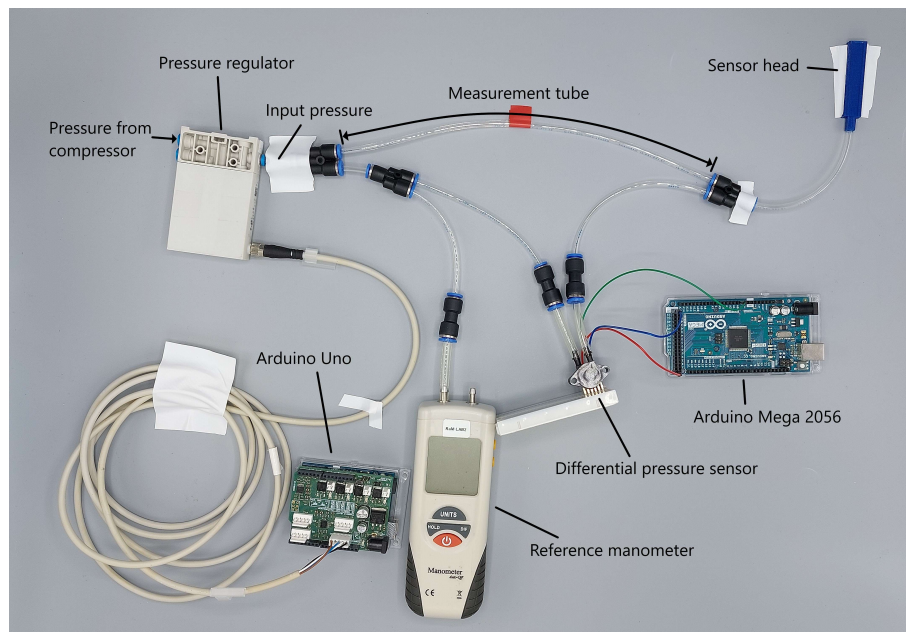


Figure 3.1: Setup of pneumatic tubing. The connection between Arduino's and PC and the pneumatic connection to the compressor have been omitted. The input pressure and measurement tube indicated in the figure correspond to the definitions as used in section 3.4

To regulate the input pressure, an Arduino Uno (Arduino, Somerville, MA, USA) controls a pressure regulator of type VEAB-L-26-D7-Q4-V1-1R1 (Festo, Esslingen, Germany). This pressure regulator has an internal pressure sensor that is used to measure the input pressure. Additionally, a HT-1890 manometer (Dongguan Xintai Instrument, Dongguan, China) was set up for reference. The output of the differential pressure sensor was recorded at about 1800 Hz using an Arduino Mega 2560 (Arduino, Somerville, MA, USA). Recordings of ten seconds were taken at each position.

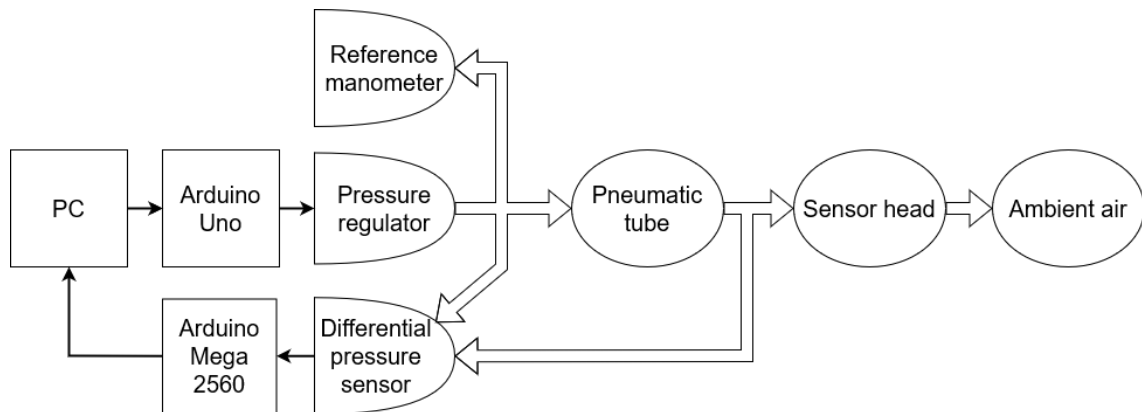


Figure 3.2: Schematic diagram of the measurement setup. Electronic components are indicated with squares, pneumatic components with ovals. Electronic interactions are indicated with thin arrows and pneumatic interactions are indicated with wide arrows.

To control the extension of the sensor, the outer tube of the sensor head was clamped horizontally, such that the inner tube could slide within (figure 3.3). Using a caliper, the distance from one end of the inner tube to the other end of the outer tube could be prescribed.

Any deviations from this setup are mentioned in their respective sections.

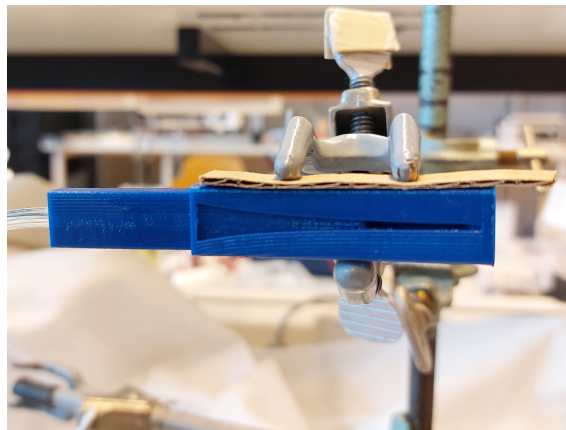


Figure 3.3: Prototype 3 clamped during measurements.

3.2 Sensor material

To ensure that the materials are MR-Safe, the parts that are required to be inside the MRI-scanner will be made out of plastics. This will include standard polyurethane pneumatic tubing and 3D-printed materials. During prototyping, the performance of three different materials is tested: polyactic acid (PLA), VeroWhite and acrylonitrile butadiene styrene (ABS). In this project, pneumatic fittings are used that do contain conductive materials. However, these are positioned at locations that are envisioned to be outside of the MRI-room during scanning. This requires longer pneumatic tubes than demonstrated in this project.

3.3 Sensor Design

As mentioned before, the design process will be based on prototyping. Section 3.3.1 describes the design of the sensor head and how an appropriate encoder hole can be designed. Section 3.3.2 describes the practical design changes in each prototype.

3.3.1 Sensor head and encoder hole

Section views of the sensor head are displayed in figure 3.4 and 3.5. The sensor head is designed as follows. As its basis, there is a rectangular tube (inner tube in the picture) that is closed off on one side and has a circular opening on the other side, to connect a pneumatic tube to it. At the closed end of the rectangular tube, perpendicular to the length of the tube, there is a narrow slit that stretches across the full width. Across the rectangular tube slides another tube (referred to as outer tube). This tube also has a slit in it, though it is oriented in longitudinal direction. Also, this slit varies in width. This slit of increasing width will be referred to as the 'encoder hole' as it converts the relative position of the two tubes into the orifice area. The pressurised air can only flow through the orifice that is formed by overlapping of the slit of the inner and outer tube. As the outer tube slides across the inner tube, the amount of overlap varies and thus the resistance to airflow varies. Additionally, the gap inside the outer tube is covered by a duct to prevent objects on the side of the sensor, like part of the robotic structure, to interfere with measurements.

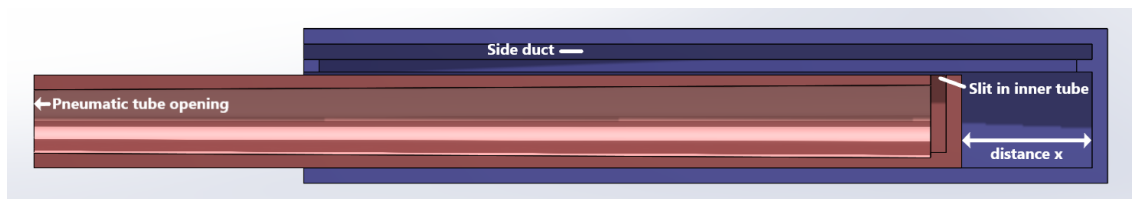


Figure 3.4: Section side view of the initial sensor design made in SOLIDWORKS (Dassault Systèmes, Vélizy-Villacoublay, France). A pneumatic tube is inserted on the left side of the inner tube (red). Air will flow from the inner tube to the side duct in the outer tube (blue) via the small slit in the side of the inner tube.

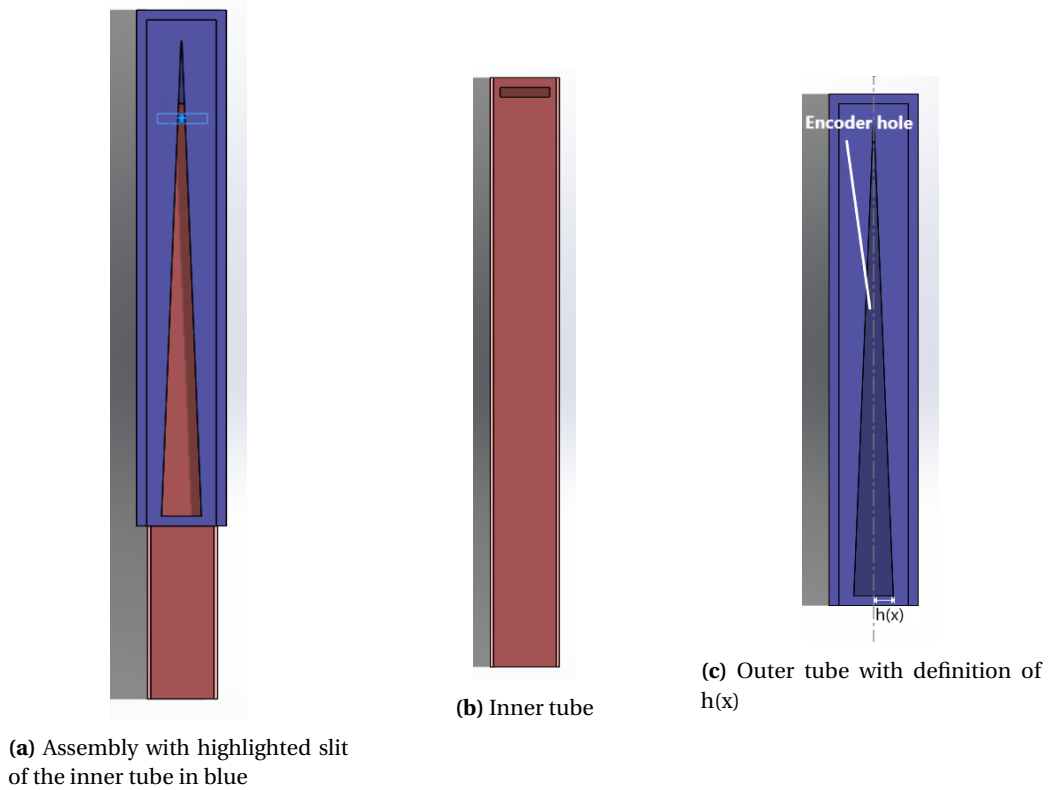


Figure 3.5: Section top view of the initial sensor design made in SOLIDWORKS (Dassault Systèmes, Vélizy-Villacoublay, France). Changing the relative position of the inner and outer tube changes the overlap of the slit on the inner tube and the encoder hole.

Encoder hole

Ideally, the position sensor is linear. Since a linear sensor will be used to measure the differential pressure, a linear relation between the measured position and the pressure difference across the tube should be established, as per equation 3.1. In this equation, the pressure drop is modeled as a function of the area of the orifice A , which is modulated by the position of the actuator x .

$$\Delta p_1(A(x)) = ax + b \quad (3.1)$$

However, the relation between the pressure drop across the tube and the area of the constriction is not linear. This means that the area of the constriction should not vary linearly as the encoder slides across it, but instead $A(x)$ follows a more complex relation. The property of the inverse of a function $f(x)$, equation 3.2, can be used to find $A(x)$.

$$f^{-1}(f(x)) = x \quad (3.2)$$

Applying this to the function $\Delta p_1(A(x))$ gives equation

$$\Delta p_1^{-1}(\Delta p_1(A(x))) = A(x) \quad (3.3)$$

By measurements, a relation can be found for $\Delta p_1(A)$ and its inverse $\Delta p_1^{-1}(A)$. Depending on the chosen function $\Delta p_1(A(x))$ (equation 3.1), the required $A(x)$ can be derived to achieve a linear sensor. Since the Δp_1 is measured using a linear sensor, equation 3.3 can be transformed

into equation 3.4, which is more directly applicable to the output of the differential pressure sensor. Here, $U(A)$ is the output voltage of the sensor as a function of the orifice area.

$$\Delta U^{-1}(\Delta U(A(x))) = A(x) \quad (3.4)$$

The area alone does not define the total geometry of the encoder. Choosing the geometry such that the encoder opening is symmetrical about its centre line, the geometry of the encoder can be described by a height function $h(x)$, which is the distance from the centre line to the edge of the opening. Furthermore, the area of the constriction also depends on the width of the slit in the sensor head w . The total area of the constriction is given by equation 3.5. To find a relation to the height function $h(x)$, this equation can be differentiated to find equation 3.6.

$$A(x) = 2 \int_x^{x+w} h(x') dx' \quad (3.5)$$

$$\frac{dA(x)}{dx} = 2(h(x+w) - h(x)) \quad (3.6)$$

Here an issue arises, because equation 3.6 does not have a unique solution for $h(x)$. This can be understood from the fact that the equation merely describes the change of area that is caused by the change of the profile as the encoder slides across the slit. Compare two situations: In the first instance, $h(x)$ is constant on the interval $x \in [0, w]$. As the encoder slides across, the trailing edge of the constriction remains at that constant height. Therefore, the entire change of area that is demanded by equation 3.6 has to be realised by a changing height at the leading edge. Now for the second situation, consider that $h(x)$ is a linearly increasing function on the interval $x \in [0, w]$, such that the initial constriction area is equal to first situation. Now as the encoder slides across, the trailing edge increases in height. To meet the demands of equation 3.6, the leading edge should now increase less.

The geometry of any interval $h(x)$ with $x \in [x, x+w]$ can be chosen to determine the total function $h(x)$. However, it is desirable to have a smooth function to limit the effect of manufacturing inaccuracies on the pressure difference. This may be achieved by utilising the function $A(x)$ itself. Let us choose $h(x) = kA(x)$, where k is a constant, resulting that the right side of equation 3.6 is as in equation 3.7.

$$2(h(x+w) - h(x)) = 2k(A(x+w) - A(x)) \quad (3.7)$$

Comparing equation 3.7 to the definition of the derivative of $A(x)$ in equation 3.8, the similarities are obvious.

$$\frac{dA(x)}{dx} = \lim_{\Delta x \rightarrow 0} \frac{A(x+\Delta x) - A(x)}{\Delta x} \quad (3.8)$$

By choosing w sufficiently small and choosing $k = \frac{1}{2w}$, the right hand side of equation 3.6 approaches the left hand side. The extend to which this holds depends also on the linearity of $A(x)$. It can empirically be verified whether choosing $h(x) = \frac{1}{2w} A(x)$ suffices. As mentioned before, to find the geometry that linearises the sensor, measurements need to be done. A prototyping sequence will be performed to improve the sensor design.

3.3.2 Sensor iteration

The following section describes the fabrication process and incremental design changes that have been made between each of the prototypes. The printed sensor heads are displayed in figure 3.6.

First prototype

The aim of the first prototype is to show the feasibility of the working principle and to derive a geometry of the encoder hole that results in a linear sensor. Therefore, a simple triangular shaped encoder hole is used. In this way, the area of the orifice can be changed linearly as a function of the distance that the outer tube moves along the inner tube. Through simple geometric analysis it can be derived that the area should then change according to equation 3.9, where x is the displacement, $\frac{dh}{dx}$ is the slope of the height profile and w the width of the slit on the inner tube.

$$A(x) = \frac{dh}{dx} \cdot (w^2 + 2wx) \quad (3.9)$$

To keep the sensor reasonably small, the maximum width of the slit is chosen the same as the outer width of the pneumatic tube, which is 4mm. Additionally, to reduce printing time in this stage of the project, the total length of the encoder hole is set at 50mm, which is below the intended range of the final product.

In the first phase of the project, two fused deposition modeling (FDM) 3D printers were available for the fabrication of the sensor head; the Ultimaker S5 (Ultimaker, Utrecht, The Netherlands) and the Ultimaker 2 (Ultimaker, Utrecht, The Netherlands). The inner rectangular tube of the sensor head is challenging to print using FDM, because it contains two perpendicular cavities. Various orientations of printing have been tried on both printers. The best results were achieved by printing the parts of the sensor head vertically, with a brim for stability. The Ultimaker S5 was able to reproduce the desired geometry of the slit better than the Ultimaker 2, with less burring. Comparative pictures of how the Ultimaker 2 and the Ultimaker S5 could fabricate the slit are in appendix A. A tolerance of +0.2 mm was used on the inner cavity of the outer tube to allow the inner tube to slide smoothly.

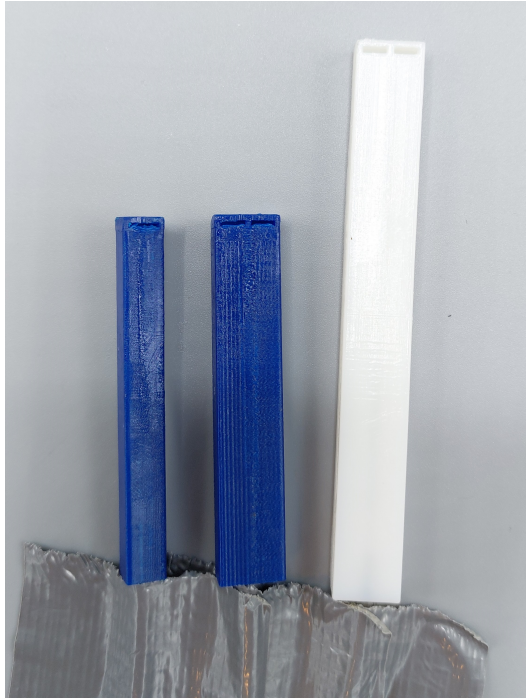
The pneumatic tube was glued to the inside of the inner tube of the sensor head to create an airtight seal.

Second prototype

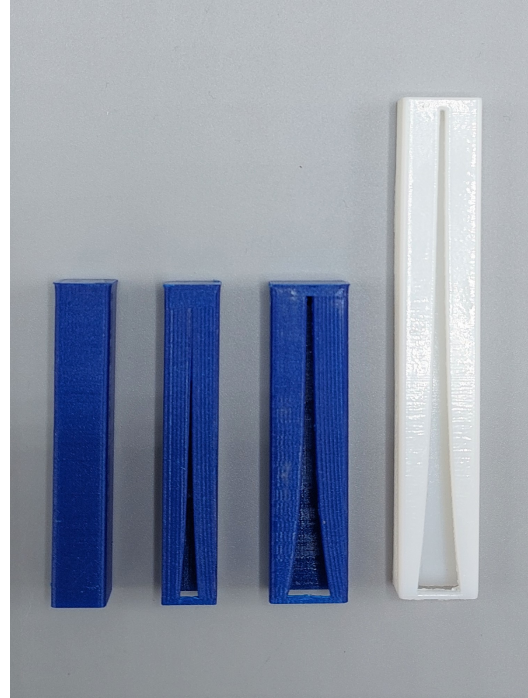
The goal of the second prototype is to validate the geometry found using the results of the first prototype that should linearise the sensor response to displacements. The method of how a geometry that linearises the sensor can be derived from the function $U(A)$ is described in section 3.3.1. Executing this method first requires a function $U(A)$, which is fitted in figure 4.2.

Based on this model, the required geometry can be produced given a desired $U(x) = ax + b$ (see equation 3.1 and 3.4). In choosing slope a and offset b , a few factors are considered. Firstly, since it is now known that the height function $h(x)$ will be an inverted exponential, the height difference at small extensions will be small, which may be problematic to reproduce with the available 3D printer. Therefore, a larger slope of the height function (large $\frac{dh}{dx}$) at small extensions is desirable. Secondly, the maximum of $h(x)$ must be at most 2 mm, as to keep the printing dimensions consistent with the model in figure 4.2. Thirdly, the values of the chosen function $U(x)$ should be within the measured values of figure 4.2 as to prevent extrapolation, since the model may not accurately describe the physics outside of the measured region. Finally, the sensitivity of the sensor is optimised by choosing a largest slope a as possible given the previous constraints.

These factors lead to a trade-off between robustness to fabrication inaccuracies and sensitivity of the position sensor. The effects of printing inaccuracies on the sensor output are not quantified in this project, which prevents the determination of optimal offset and slope of $U(x)$. Moreover, optimal parameters may vary between different prototypes, as the scaled up prototype (prototype 4) is produced with a higher quality 3D printer. This means that the scaled up



(a) Inner tubes of the prototypes. The first and second prototype share the same inner tube. From left to right: prototype 1 and 2, prototype 3, prototype 4 (scaled up version).



(b) Outer tubes of the prototypes. The first prototype was made with a cover over the slit which blocks the view on the encoder hole. From left to right: prototype 1, prototype 2, prototype 3, prototype 4 (scaled up version)

Figure 3.6: Inner and outer tubes of the different prototypes. The first three prototypes are made out of PLA. The fourth prototype is made out of VeroWhite.

prototype may improve on fabrication quality but reduce the sensitivity of the sensor. Comparing combinations of ten different values for a between 0.006 V/mm and 0.02 V/mm and ten different values for b between 2.5 V and 3.5 V on the aforementioned criteria has led to the choice of $U(x)$ as shown in equation 3.10.

$$U(x) = 3.39 + 0.0091x \quad (3.10)$$

As mentioned in section 3.3.1, this function can be used to find the approximate height profile $h(x)$ that should achieve the output of the sensor to equation 3.10. Equation 3.9 and the model in figure 4.2 can be used to assess how well this height profile reproduces the desired orifice area and in turn the desired voltage output. A width of 1 mm is chosen and indeed it turns out that this error is minimal, see figure 3.7.

Finally, the side duct that aimed to protect the airflow from influences from the side was removed, leaving the encoder hole visible for inspection. This is done to better assess the printing quality of the sensor.

The fabrication process is identical to that of the first prototype, though only the outer tube of the sensor head is printed.

Third prototype

Experiments on the first and second prototype have raised suspicions that printing inaccuracies in the inner tube of the sensor have led to nonlinearities in the sensor output. The goal of the third prototype is to correct for these errors.

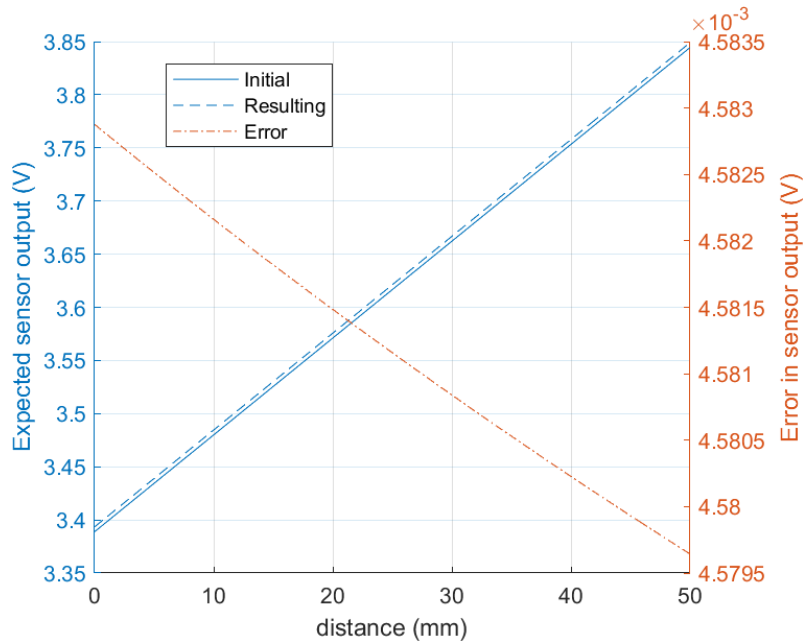


Figure 3.7: Difference between desired voltage output and voltage output given the selected $h(x)$ according to the power model, using a slit width of 1 mm.

As mentioned before, printing the slit on the side of the sensor head using FDM is challenging. Since the surface area of this slit is so small, tiny deviations from the intended geometry will propagate to cause large linearity issues. To mitigate this issue, the slit is made wider. However, to prevent the printer to bridge across even larger distances, a supporting piece of PLA is printed in the middle of the slit, effectively forming two separate slits. This material is not removed, but instead the height profile $h(x)$ is offset by half the distance of this support. Additionally, $h(x)$ is scaled up by a factor of two, since there are now two slits to cover instead of one.

Both the inner and outer tube of the sensor head are reprinted via the same method as the first prototype.

Upscaling

After linearising the sensor and improving its sensitivity, the sensor should be scaled up to accommodate different pneumatic motors. In this phase of the project, new fabrications options were available to produce the prototypes.

The fourth prototype is scaled up by 60% compared to the previous prototypes, such that it should have a range of 70 mm. This is achieved by scaling the previously found height function 60% in x -direction. This means that the height changes even more subtly along the length of the encoder hole than before. Therefore, two different fabrication methods have been tested.

The Object 260 Connex3 (Stratasys, Rehovot, Israel) has been used to produce the scaled up version using the material VeroWhite. The Connex3 is a PolyJet printer, which means that it creates its parts by jetting photopolymer resin into a desired pattern and curing it using UV light. For consistency among prototypes, the sensor head is only scaled up in length and no other changes are made to the design.

The outer tube of this prototype was found to be a bit flexible, so this outer tube was reprinted using the Fortus 250mc (Stratasys, Rehovot, Israel) using the material ABS. This time, the wall thickness of the outer tube was increased to 2 mm to improve rigidity. Additionally, it was found that the encoder hole was printed a bit too narrow at the small edge (see appendix A).

Therefore, in the ABS print, the height function was offset by an additional 0.05 mm (which is a total increase of 0.1 mm to the width of the encoder hole).

3.4 Parametric analysis

To optimise the sensor, it should be considered which parameters make the differential pressure sensor most sensitive to the modulation of the flow. Therefore, this section discusses how two parameters can be chosen to optimise sensor sensitivity.

The parameters are selected using equation 2.5. This equation shows that the relevant parameters for the pressure drop across the measurement tube are the mean air velocity V , the air density ρ , the ratio of length and diameter of the measurement tube L/d , the relative roughness of the measurement tube ϵ/d and the Reynolds number Re . It is difficult to control each parameter individually, so instead the effect of related parameters that are easily controlled by the operator of the sensor is investigated.

The first parameter is the input pressure. This parameter is expected to affect the Reynolds number, air density and mean air velocity. The input pressure is defined as the gauge pressure that is regulated at the upstream end of the differential pressure measurement (see Figure 3.1).

The second parameter is the measurement tube length. This will mostly affect the ratio L/d , but in part also the Reynolds number, air density and mean air velocity because the introduction of additional resistance. The measurement tube length is defined as the length of the pneumatic tube across which the differential pressure is measured (see Figure 3.1).

3.4.1 Parameter value selection

To investigate the effects of input pressure on the sensor output, measurements are done for seven different input pressures: 0.035 bar, 0.073 bar, 0.112 bar, 0.149 bar, 0.189 bar, 0.229 bar and 0.268 bar. The tube length is 50 cm for all these measurements.

To investigate the effects of tube length on the sensor output, five pieces of pneumatic tube are used, each with a different length: 10 cm, 30 cm, 50 cm, 70 cm and 90 cm. The pressure is set at 0.150 bar for all the tube lengths.

Additionally a third set of parameter combinations of pressure and tube length are measured. This set contains all aforementioned tube lengths, but the pressure is chosen such that the output of the differential pressure sensor is almost clipping (remains at 4.9 V) when the outer sensor head tube is removed from the inner tube. The pressures associated with the tube lengths are 0.39 bar, 0.29 bar, 0.23 bar, 0.21 bar and 0.19 bar, listed in order of ascending tube length.

At each combination of tube length and input pressure that is tested, a characterisation of the sensor output is measured using six different displacements spaced approximately equally along the range of 45 mm. Each measurement is performed three times. The measurements are performed on the third prototype, which was described in section 3.3.2.

3.5 Sensor Characterisation

To conclude this project, some additional measurements are done on the final product. Since the scaled up versions are not yet functioning properly, the measurements are done on the third prototype produced on the Ultimaker S5. The following characteristics will be determined.

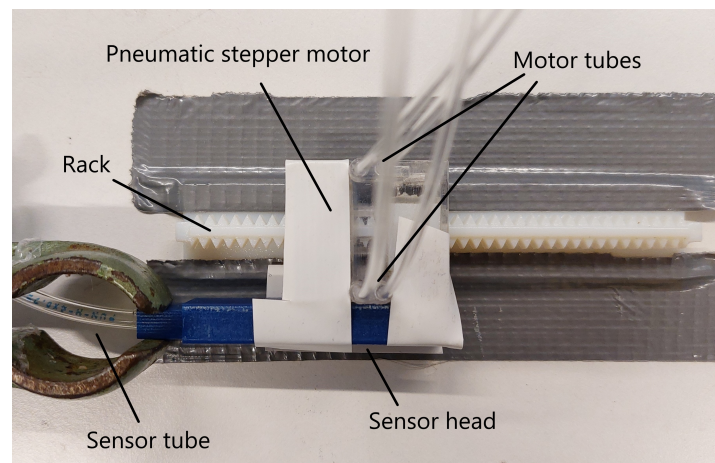
- Precision
- Sensitivity
- Accuracy
- Linearity

For determining the precision, sensitivity and linearity, the results of the parametric analysis will be used. Figure 4.4c shows that there are many options to choose the input pressure and tube length to achieve a similarly high sensitivity. Though the confidence intervals are large and no definitive conclusions can be drawn, there may be a slightly higher sensitivity for shorter tube lengths with higher pressure. There is no evidence for a sensitivity gain for tubes shorter than 30 cm, so a pressure of 0.29 bar and a tube length of 30 cm was used.

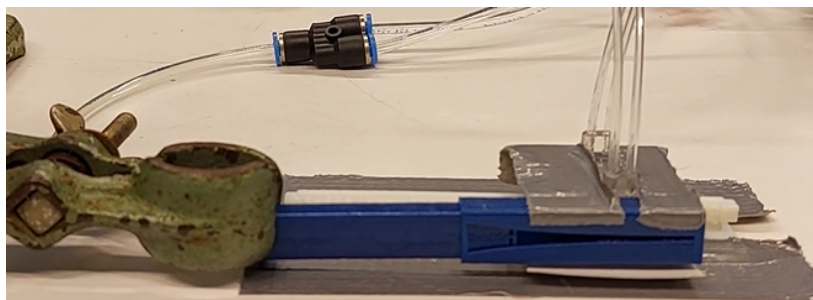
For the precision measurement, fifteen measurements were done at each of six different extensions across the range. This then also results in a relation that allows to determine the sensitivity. The sensitivity of this setup was tested before in the parametric analysis, but the larger quantity of measurements in this experiment allows for less uncertainty on the result.

For the linearity measurement, a higher resolution is required, so measurements are taken with a spacing of 1 mm. Again, measurements are repeated three times. The linearity is defined as the (relative) maximum deviation from the input of the sensor. That is, the maximum distance the measurements deviate from the reference line in horizontal direction, since this will be the error when determining the position from a certain output voltage.

The accuracy will be tested in a different setup that resembles the intended application of the sensor. A pneumatic stepper motor of the same type as used in the robot by Shametaj (2021) was placed on a rail that was fixed to the table. The outer tube of the sensor was then attached to the actuator using duct tape. The inner tube was clamped and placed such that it was parallel with the rail along which the stepper motor moved. The motor was then moved along the rail and differential pressure was recorded for ten seconds at positions uniformly distributed along the range. The displacement of the actuator was measured using calipers. Pictures of the setup are in figure 3.8.



(a) Top view of the measurements on the pneumatic stepper motor.



(b) Side view of the measurements on the pneumatic stepper motor

Figure 3.8: Experimental setup for tests on prototype 3 using a pneumatic stepper motor

To calculate the position back from the averaged differential pressure signal, the linear fit through the data points used for calculating precision is used. To calculate the position from the measured voltage, two methods are compared.

The first method uses the best linear fit that is found through the characterisation directly. The second method uses normalisation to attempt to compensate for small differences in conditions between the measurement of the reference line and the application of the sensor. In this method, the reference line is made on normalised data; both the voltage and distance are normalised according to equation 3.11. Here y_{min} is the value of the quantity at the low end of the range and y_{max} is the quantity of the value at the high end of the range. Next, before measuring on the stepper motor, the voltage is also measured at the low end and high end of the range. This is then used to normalise the data from the measurement on the stepper motor, also according to equation 3.11. The normalised reference line can then be used to estimate the position to be measured using equation 3.12, where x_{est} is the estimated position (mm), U_{norm} the normalised voltage, x_{max} the range of the sensor (mm), and a is the slope of the normalised reference line and b its offset.

$$y_{norm} = \frac{y - y_{min}}{y_{max} - y_{min}} \quad (3.11)$$

$$x_{est} = \frac{U_{norm} - b}{a} \cdot x_{max} \quad (3.12)$$

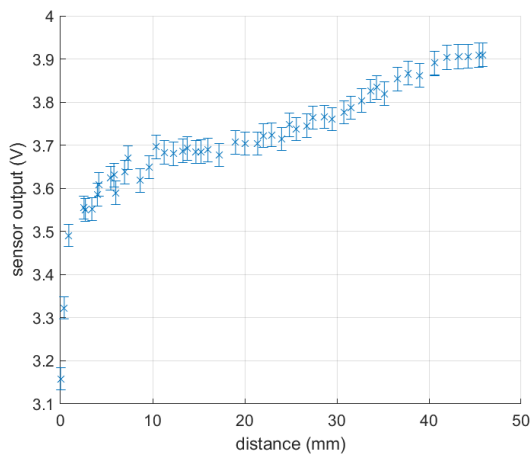
4 Results and discussion

This section displays the results from the various experiments and discusses them. All fits were weighted using the inverse of the width of the error bar of each data point.

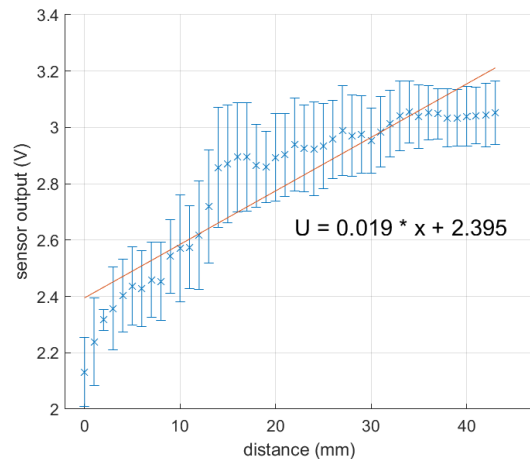
4.1 Sensor iteration

Figure 4.1a shows the average voltage output measured over ten seconds as a function of the extension of the sensor head. Figure 4.2 displays again the average voltage output, but plotted against the estimated orifice area. Indeed the data follows the same distribution as in figure 4.1a, though the horizontal axis is scaled differently and slightly offset. This allowed for fitting an exponential curve onto the data to achieve the desired function $U(A)$.

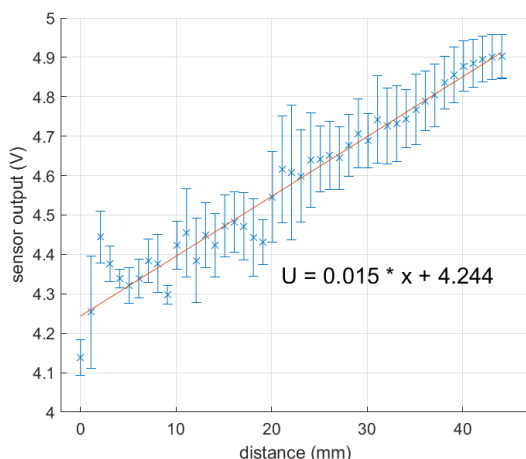
Figure 4.1b and 4.1c show the sensor output of the second and third prototype as a function of displacement and its best linear fit.



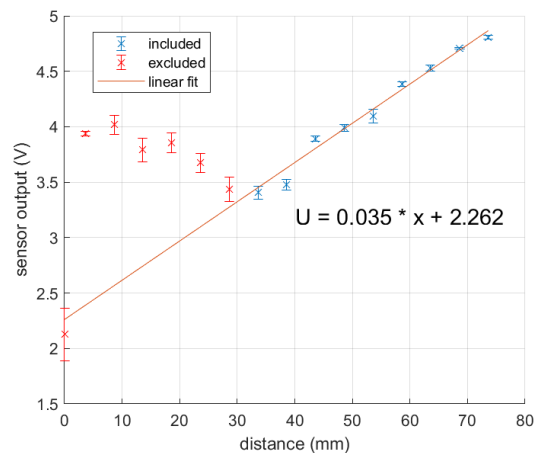
(a) First prototype. Error bars display standard deviation of each sample.



(b) Second prototype. Error bars display CI95% of the mean.



(c) Third prototype. Error bars display CI95% of the mean.



(d) Fourth prototype (VeroWhite). Error bars display CI95% of the mean. The data points below 30mm have been excluded from the fit.

Figure 4.1: Sensor output against displacement for prototype 1, 2, 3 and 4. Prototype 2,3 and 4 display their best linear fit.

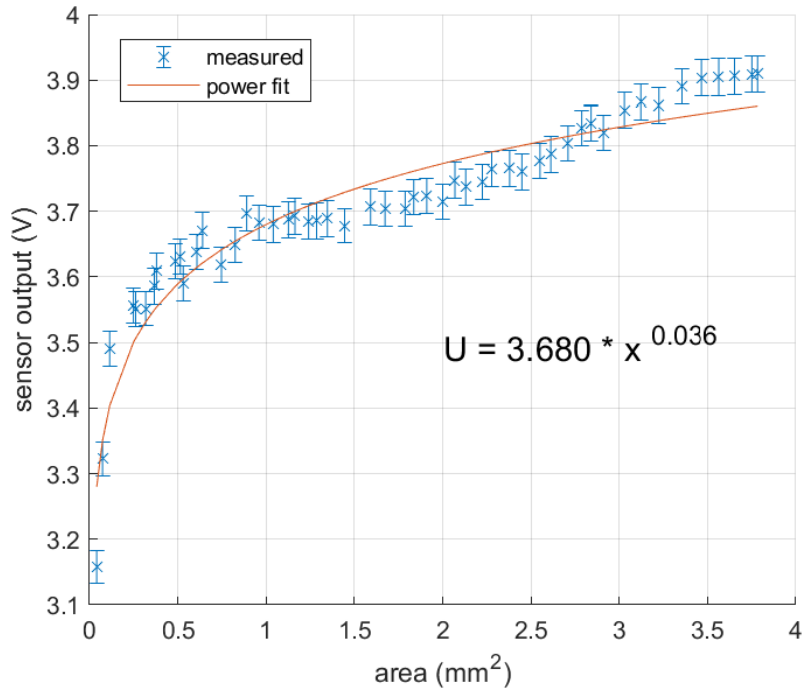


Figure 4.2: Power fit of output voltage as function of surface area. Error bars display the standard deviation in each sample. Error in the surface area is not evaluated.

Figure 4.1d shows the response of the upscaled sensor that was entirely made out of VeroWhite material. Clearly, at low extensions the sensor does not behave as intended. Therefore, extensions below 30 mm were excluded from the linear fit.

Replacing the VeroWhite outer tube by the ABS outer tube did not improve the results. In fact, extensions larger than 15 mm were indistinguishable from each other.

4.1.1 Discussion

Printing inaccuracies

The response from the first prototype (see figure 4.1a) is rather irregular, especially at small extensions the data points do not follow up each other in a consistent pattern. Also, between an extension of 10 mm and about 30 mm the data points form a concave shape which is not to be expected, since the relative increase in area of the orifice should always decrease with extension of the sensor head. A likely cause of this is inaccuracy of fabrication.

Not only is the geometry of the encoder hole important, but also the geometry of the side slit of the inner tube of the sensor head. Especially when the total area of the orifice is small, tiny variations in the geometry can disrupt the airflow. Moreover, at small extensions the middle of the slit is uncovered, while the middle part is most prone to fabrication error due to the large distance that the 3D printer has to bridge to form it.

Additionally, during measurements it turned out that the sliding tolerance allows a bit of rotational movement when the sensor head extends too far. Therefore, the maximum range is limited to 45 mm.

The response of the second prototype (figure 4.1b) seems to deviate the most from the linear fit at approximately the same relative positions where the data from the first prototype (figure 4.2) seems to deviate from its corresponding fit, though the sign of the deviation is reversed. A likely cause for this is the inner tube of the sensor head that has been used in both experiments. Inaccuracies in the fabrication of this tube were already suspected to cause these deviations from

the model in figure 4.2 and the results from the second prototype (figure 4.1b) are consistent with that theory.

The issues in the second prototype led to the design alterations in the third prototype. Though the data in figure 4.1c is not entirely regular, especially at small extension of the sensor, the deviations have indeed been reduced compared to the second prototype. Any nonlinear effects that are still present in the response may still be caused by fabrication inaccuracies.

Leakage

Furthermore, the responses of the first and second prototype (figure 4.1a and 4.1b) are overall lower than that of the third (figure 4.1c). This is attributed to a leak in the system that was discovered some time after these measurements were made. The leak was caused by an incorrectly cut pneumatic tube that did not fit correctly into the pneumatic fitting. The leak was located very close to the pressure regulator. This caused the effective pressure to be lowered by an unknown amount. This is not necessarily problematic, since the influence of this parameter is investigated in the parametric analysis.

Linearisation process

Throughout the linearisation process in the first three prototypes, there were several inconsistencies in that may have introduced errors in the geometry of the design. Firstly, the initial design was produced with a longitudinal duct over the encoder hole. The intended purpose of this duct was to prevent objects on the side from interrupting the airflow. However, this made inspection of the encoder geometry very difficult, so it was removed from the second prototype on.

Ideally, the relation $U(A)$ should have been measured again before computing the desired geometry. Additionally, for characterising this relation $U(A)$ a more robust setup could have been built. The setup that was used was based on the sensor design itself. However, for these measurements, the two-component sensor head was not yet required and instead several different orifice sizes could be printed in such a way that no bridging is required. This reduces the uncertainty of the orifice area in the measurements. Ideally, a high quality printer would be available right from the start of the project to ensure that this model, which forms the basis of the design of further sensors, is accurate.

Challenges printing on a different machine

Regarding the upscaled design, considering the slope of the fit in figure 4.1d, the sensitivity loss is indeed expected to be close to 60%, because the same orifice modulation is spread out over a 60% larger range compared to previous prototypes.

The response from the upscaled prototypes shows that producing the sensors on the higher quality 3D printers has had more effects than merely an improvement in the accuracy of the geometry. The first three prototypes were fabricated on the exact same machine. Transferring the same 3D model to a different machine may cause differences due to different calibrations and accuracies. Moreover, these printers cannot use the same materials and the Connex3 uses an entirely different printing technique (PolyJet instead of FDM).

Deviations at small sensor extension

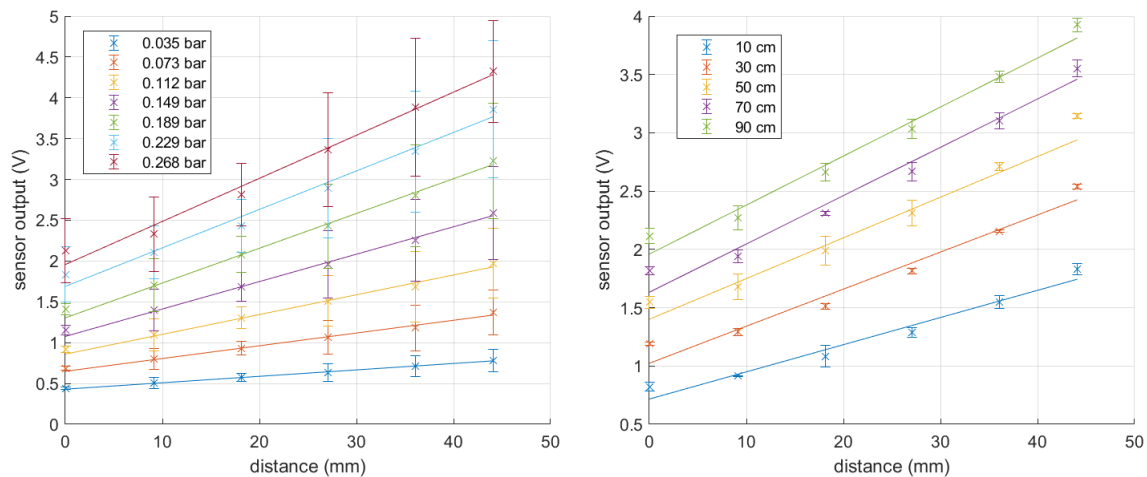
The apparent downward trend for small extensions in figure 4.1d does not appear to be related to geometrical inaccuracies in the encoder hole itself. The hole is clearly smaller at 10 mm from the narrow edge than at 50 mm from the narrow edge, even though these positions result in a similar output. Possibly, this is related to the interface of the inner tube and outer tube. If the flexibility of the tube allows the encoder hole to exhibit too much sag, it could prevent the slit on the inner tube from being covered adequately. This would cause ducts to form at the sides of the slit, allowing more air to pass through. The amount of sag could decrease with

distance, since the length of the inner slit to be covered decreases, which would explain why this undesired behaviour occurs only at small extensions.

To test this idea, a new prototype should be made on the same machine that is more rigid. Unfortunately, the Connex3 went out of service shortly after testing the prototype. As an alternative, the Fortus was used to produce the aforementioned ABS version of the outer tube. This is not ideal, since this means that again differences are introduced due to using a new material, printing technique and possible calibration differences. Indeed it turned out that the sensor response was entirely different. It appears to leak a lot of air through other ways than the encoder hole. Inspecting the outer tube shows that there appear to be some small holes at the edge of the encoder hole (see appendix A), which may cause the leakage. Other printing settings could be investigated to make sure that the walls are airtight.

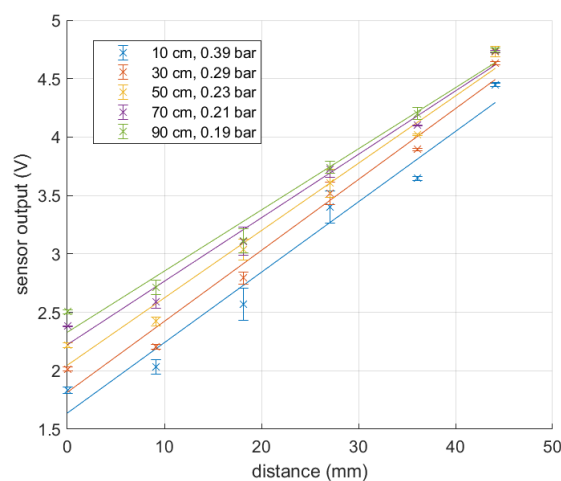
4.2 Parametric analysis

Figure 4.3b, 4.3a and 4.3c show the response of the sensor for the different combinations of input pressure and tube length.



(a) Different measuring tube lengths at an input pressure of 0.150 bar

(b) Different input pressures at a measuring tube length of 50 cm

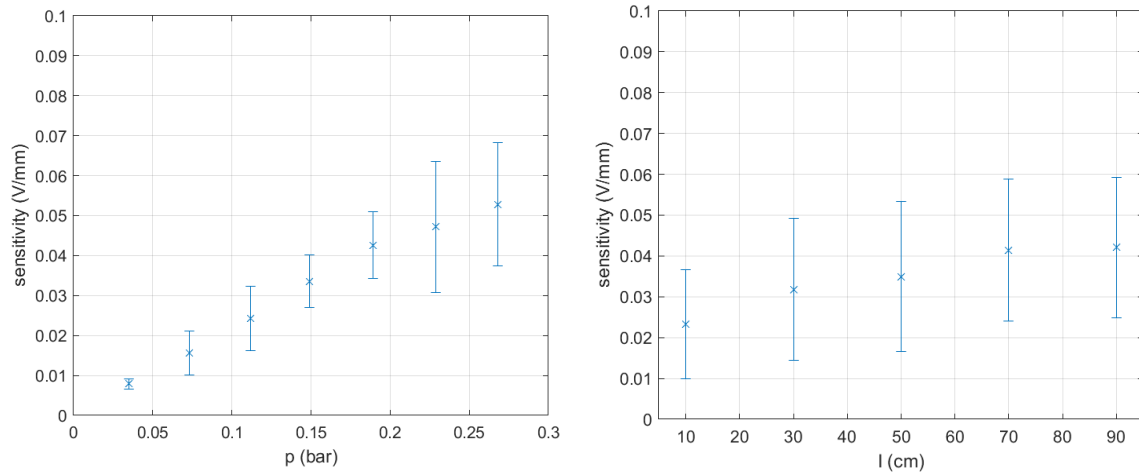


(c) Combinations of tube lengths and input pressures that saturate the differential pressure sensor when the outer tube is removed (maximally allowed pressure)

Figure 4.3: Sensor behaviour for different combinations of input pressures and tube lengths. Error bars display CI95% of the mean.

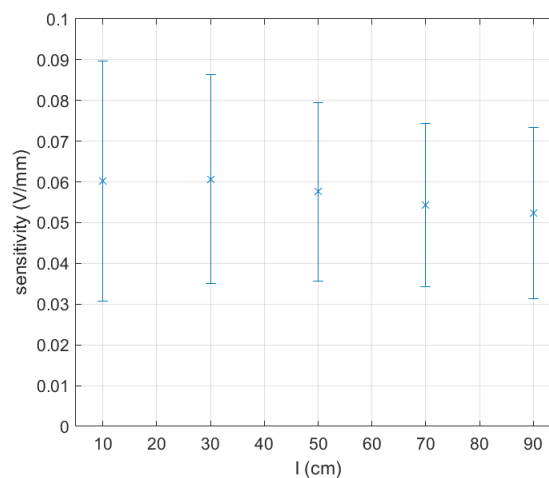
For each combination of pressure and tube length, the slope and the offset of the sensor response are determined by the best linear fit. Corresponding figures displaying, the change in sensitivity (slope) and offset in figure 4.3 and 4.5.

To obtain a more general insight into the relation between the two parameters and the sensitivity of the sensor, a first order multiple regression is applied on both the sensitivity and the offset. Appendix B shows the three dimensional plots of this regression. The model is shown in table 4.1.



(a) Different input pressures with a tube length of 50 cm

(b) Different tube lengths at 0.150 bar



(c) Different tube lengths at the maximally allowed input pressure

Figure 4.4: Sensitivity measurements for different tube lengths and input pressures. Error bars display CI95% of the mean.

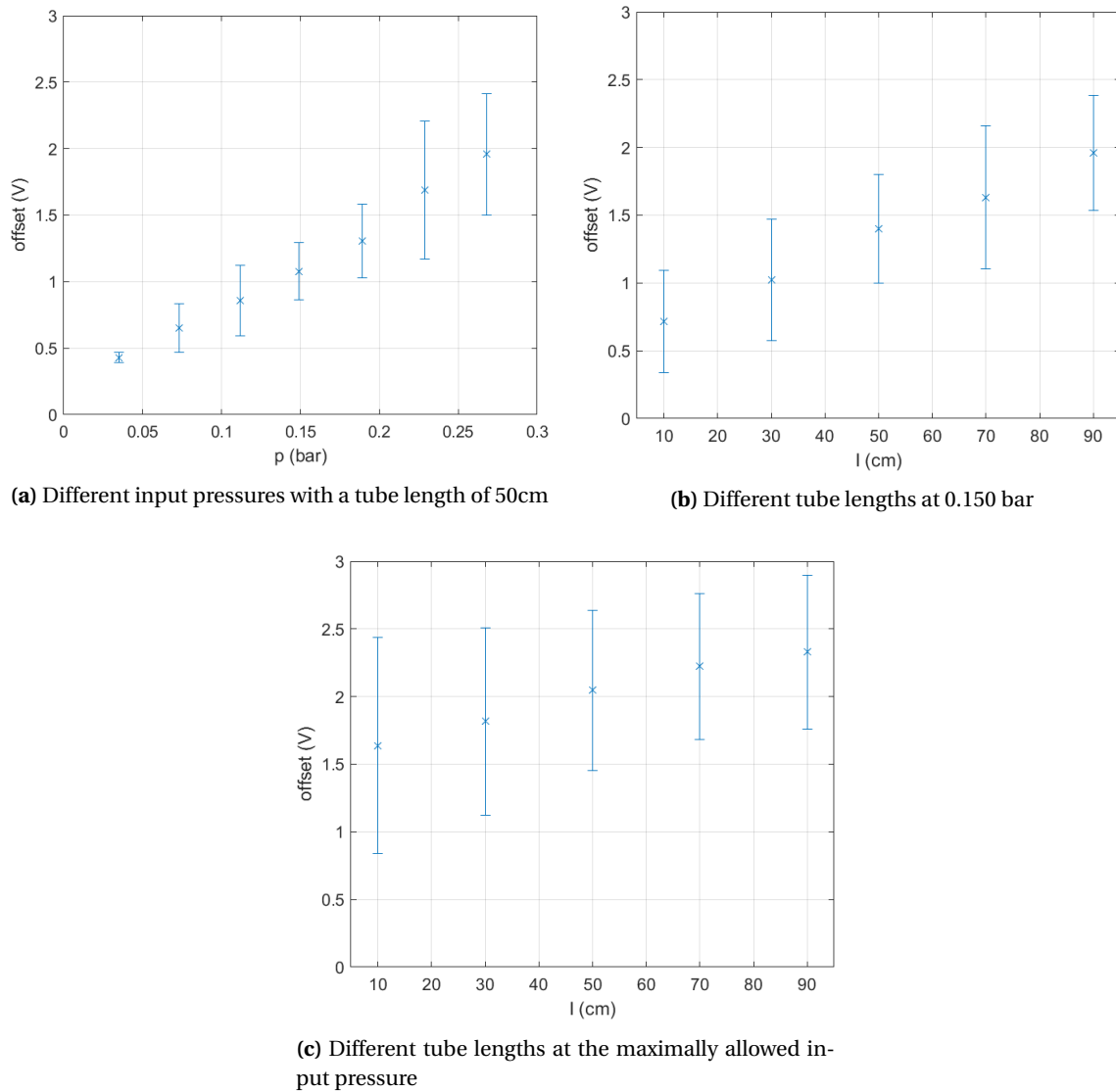


Figure 4.5: Sensor offset measurements for different input pressures and measurement tube lengths. Error bars indicate CI95% on the mean.

Table 4.1: Best fit for sensitivity and offset using the model $Y(L,p)=a+bL+cp$, where $Y(L,p)$ is the sensitivity or offset as a function of tube length and pressure. L is in cm and p in bar.

Table 4.2: Model for sensitivity

a (V/mm)	-0.0134
Min CI95%	-0.0195
Max CI95%	-0.00737
b (V/mm/cm)	$2.91 \cdot 10^{-4}$
Min CI95%	$1.86 \cdot 10^{-4}$
Max CI95%	$3.96 \cdot 10^{-4}$
c (V/mm/bar)	0.211
Min CI95%	0.193
Max CI95%	0.229

Table 4.3: Model for offset

a (V)	-0.731
Min CI95%	-1.01
Max CI95%	-0.448
b (V/cm)	0.0189
Min CI95%	0.0141
Max CI95%	0.0237
c (V/bar)	6.65
Min CI95%	5.78
Max CI95%	7.52

4.2.1 Discussion

Judging by figure 4.3b and 4.3a, larger input pressure and longer tubes increase the slope of the sensor response and thus the sensitivity. This allows for the optimisation of the sensitivity by means of parameter tuning. The choice in parameters is limited by the output saturation voltage of the differential pressure sensor, which is 5V. Indeed, figure 4.3c shows that maximising pressure for a particular tube length indeed increases the sensitivity of the sensor. The sensitivity at 10 cm is hardly larger than the sensitivity at 30 cm, while the input pressure is about a third more. Therefore, the next prototype will use a 30 cm tube at 0.29 bar.

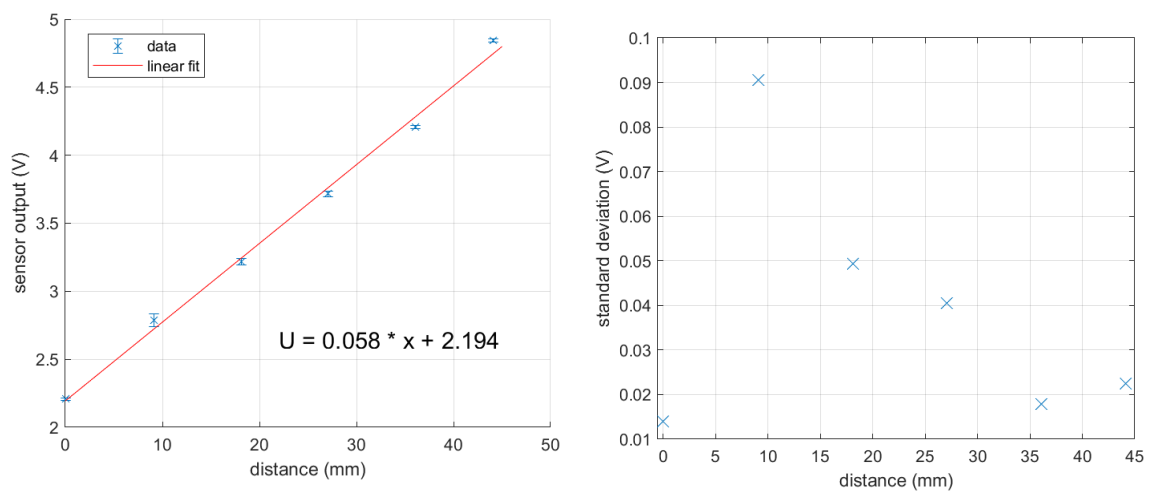
For the multiple regression, higher order regressions have been attempted, but the parameters of the resulting functions did not differ significantly from zero, so instead first order models were used. The resulting function of the sensitivity regression can be used to estimate how the sensitivity changes upon changing any of the two parameters. However, to estimate whether the maximum pressure is still in range of the pressure sensor it is important to know the offset as well. The offset regression can be used to check whether the signal is still in range of the differential pressure sensor.

Additionally, the parametric analysis would be more substantial if more data would have been gathered. Testing more combinations of pressure and tube length can give a definite answer whether the best fit of these parameters is indeed linear. This is not to be expected, since the resulting linear fit of the sensitivity has an offset. This is unrealistic, since an input pressure of 0 bar and a tube length of 0 cm could never result in any finite sensitivity. Unfortunately, these measurements are time consuming since each data point requires an entire characterisation of the sensor response.

4.3 Sensor characterisation

Figure 4.6a shows the response of the final product. From the linear fit it can be derived that the sensitivity is 0.058 ± 0.001 V/mm (CI95%). Next, figure 4.6b displays the standard deviation at each measurement location. The maximum standard deviation observed is 0.09 V.

Figure 4.7 compares the two methods of determining the position of the sensor from the voltage measurement. Here a positive error corresponds to an overestimation of the distance by the sensor. Table 4.4 shows that the absolute mean error is almost halved by applying the normalisation while the absolute maximum error is only slightly reduced.



(a) Fifteen measurements taken at each of six different extensions of the final product. Error bars indicate CI95% on the mean.

(b) Standard deviation in the measurements at the different positions

Figure 4.6: Sensor measurements on prototype 3 to characterise precision and sensitivity.

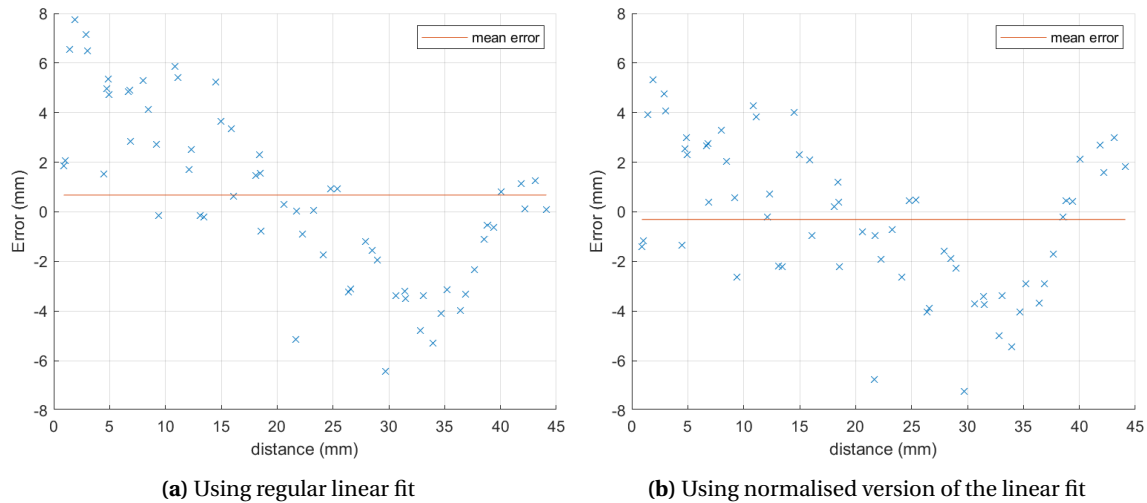


Figure 4.7: Comparison of error distributions using the regular and normalised version of the linear fit from figure 4.6a

Table 4.4: Comparative table of the effect on the accuracy using a regular linear fit and a normalized linear fit

	Regular linear fit	Normalized linear fit
Positive maximum error (mm)	7.6	5.3
Negative maximum error (mm)	-6.5	-7.2
Mean error (mm)	0.59	-0.31

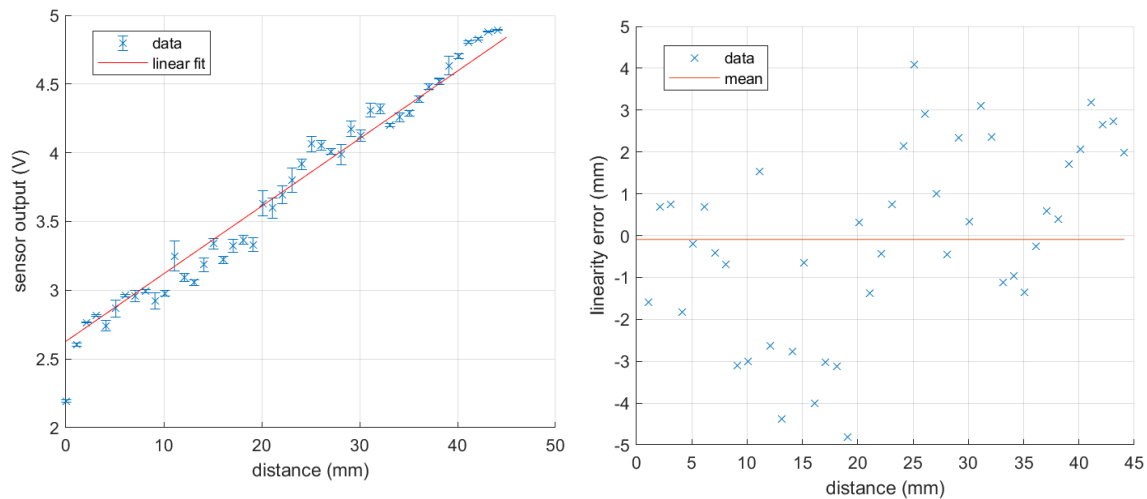


Figure 4.8: Measurement of linearity of prototype 3 at 0.290 bar with a measurement tube length of 30cm.

4.3.1 Discussion

The sensitivity of prototype 3 of 0.058 ± 0.001 V/mm (CI95%) is in reasonable agreement with the sensitivity found in the parametric analysis with the same settings (pressure of 0.29 bar and a tube length of 30 cm), which was 0.061 ± 0.015 V/mm (CI95%). Judging from the standard deviations in figure 4.6b, the precision seems to be a function of the distance. The standard deviation upon closing the sensor head (0 mm distance) is very low. This can be understood by the fact that this is a highly repeatable operation as the inner tube can be pressed against the outer tube.

For the other measuring locations it seems that lower distances have a higher standard deviation. This may be related to the fact that for smaller distances, the outer tube needs to cover a larger part of the slit in the inner tube. Hence, if the extend to which this slit is adequately covered changes per measurement, the differences will be larger for smaller distances, leading to a larger standard deviation.

As per table 4.4, using the normalised fit for determining the position from the voltage may have a slight advantage over the regular fit. It can limit the effect of slight variations in input pressure, leakage or other deviations from the conditions that were used to create the reference line. In this particular case, it reduced the average error but the absolute maximum error is hardly affected. In absolute terms, the accuracy is below the required accuracy for the intended application. Even in the best case, the maximum error is still 16.3% of the full range.

The absolute maximum linearity error is 4.7mm or 10.6% of the total range. This means that linearity is still in large part an issue for the accuracy of the sensor.

4.4 Limitations

Some factors have not been taken account in this project. For example, the influence of ambient factors like temperature was not investigated. But also more prominent aspects, like the width of the slit on the inner tube of the sensor head have only been discussed briefly. It is assumed that the orifice area is the only factor that modulates the flow rate, but it is not investigated what the contribution of the shape of the orifice is. Possibly, its influence on the flow profile could be of interest in optimising the slit width.

Finally, this project has been limited to static behaviour of the sensor. For use in robotic applications, the dynamic properties may be of significant influence on the speed of the control system. Before this sensor can be integrated in a robotic system, an analysis of dynamic effects should be done. For instance, turbulence in the sensor will cause a lower limit to the amount of measurements needed for precise position sensing. Additionally, in practice the sensor will be connected to a robot via a long pneumatic tube, which introduces delays and requires a higher input pressure due to the additional resistance. All these effects are not investigated in this project.

5 Pneumatic encoder

Previous prototypes have the disadvantage that scaling them up leads to a loss of sensitivity. Moreover, the fabrication accuracy and precision of the fabrication machinery limits the achievable accuracy of the previous prototypes. This chapter is devoted to creating a different design, based on the previous prototypes. Namely, a prototype is produced to explore the possibility of creating a pneumatic encoder.

5.1 Sensor Design

An optical encoder may measure two signals that are out of phase to determine the direction (forward or backward) and magnitude of displacement. Copying this principle to the pneumatic encoder would require two differential pressure sensors and two pneumatic tubes attached to the sensor head. This makes the sensor more expensive and bulky. Instead, the prototype makes use of one channel only. This is done by making an assumption about the actuator under measurement: it moves at a constant speed, it moves at a constant stepping frequency or it does not move. This assumption allows the additional directional information to be encoded in the rate of change of the sensor output by choosing a suitable encoder geometry. Additionally, an algorithm was designed to exploit this assumption.

In terms of the design, only the outer tube of the sensor head was changed. Instead of one encoder hole, multiple encoder holes were placed behind each other. The encoder holes were scaled down to 6 mm in length. Between each encoder hole was 1 mm, such that the total length of each segment is 7mm. The result can be seen in figure 5.1. Next, an algorithm was designed to detect transition from one segment into the next.

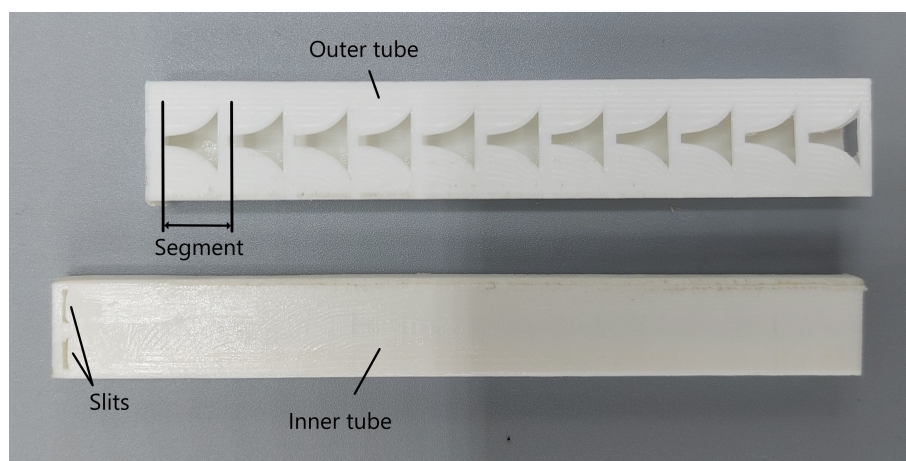


Figure 5.1: Encoder 3D printed out of PLA

The sensor response of the encoder can be modelled using the earlier derived $U(A)$ and is displayed in figure 5.2. This is used to design an algorithm for keeping track of the segment count, see figure 5.3. It makes use of the concept of 'zones', where each zone corresponds to a piece of the sensor response as a function of distance. Zone 0 is the lower half of the linear part of the response, zone 1 is the upper half of the linear part of the response and zone 2 is the steep nonlinear part of the sensor response that occurs in the transition of one segment to the next.

Transitions between the different zones are detected by using four different thresholds: a 'low threshold', 'middle threshold', 'high threshold' and 'slope threshold'. Assuming the measured actuator travels at a constant speed or stepping frequency, the maximum change of the voltage

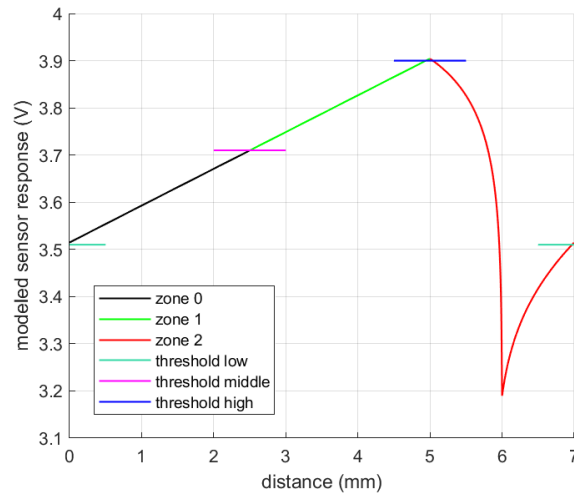


Figure 5.2: Modeled response of one segment of the encoder. Three out of four thresholds are indicated. Note that the slope threshold is not indicated since this refers to a rate of change in time, not in distance.

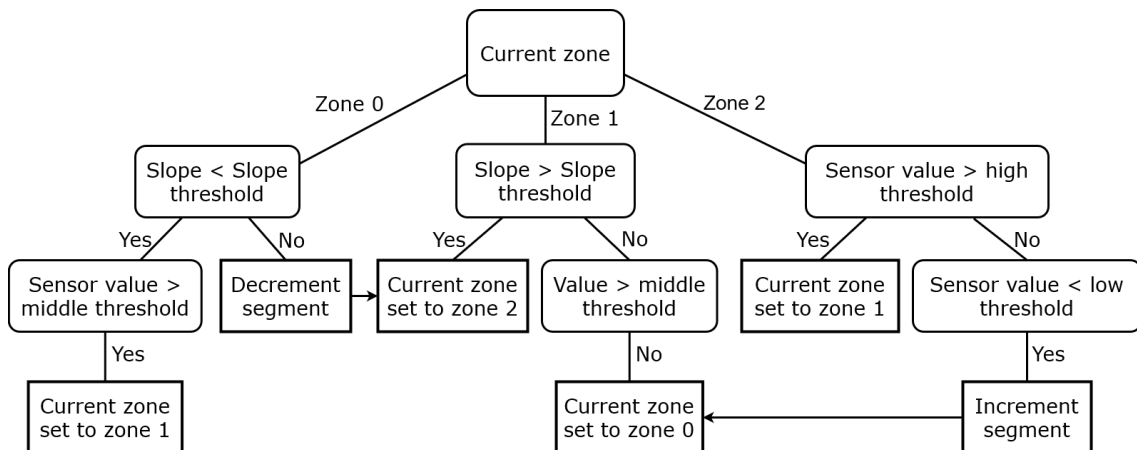


Figure 5.3: Decision tree of the algorithm that keeps track of the current segment and zone. Rounded squares are decision points and straight squares are actions to be taken. An arrow means that multiple actions will be taken in succession.

in time is limited. In zone 2, this slope will be larger than in zone 0 and zone 1. Therefore, a transition into zone 2 is detected by exceeding a certain slope threshold. Other transitions are detected by surpassing threshold values at the edges of the zone. For example, zone 0 has the low threshold at its low end and the middle threshold at its high end (see figure 5.2).

A static characterisation of the response within a segment is used to estimate the position within a segment. Since this segmented approach now results in a nonlinear response, a piecewise linear approximation is used.

5.1.1 Experiment

To test the performance of the encoder, two experiments were conducted. Firstly, the sensor response was measured statically in the same setup as used for the other prototypes (see figure 3.1 and 3.2). Measurements were taken across the three middle segments with a spacing of 0.5 mm in between measurements. This was repeated three times. The results of all three segments were averaged to result in a static characterisation of a single segment. Secondly, to determine the accuracy of the encoder, measurements were done on a pneumatic stepper motor. The encoder was taped on the motor. The setup can be seen in figure 5.4 and 5.5.

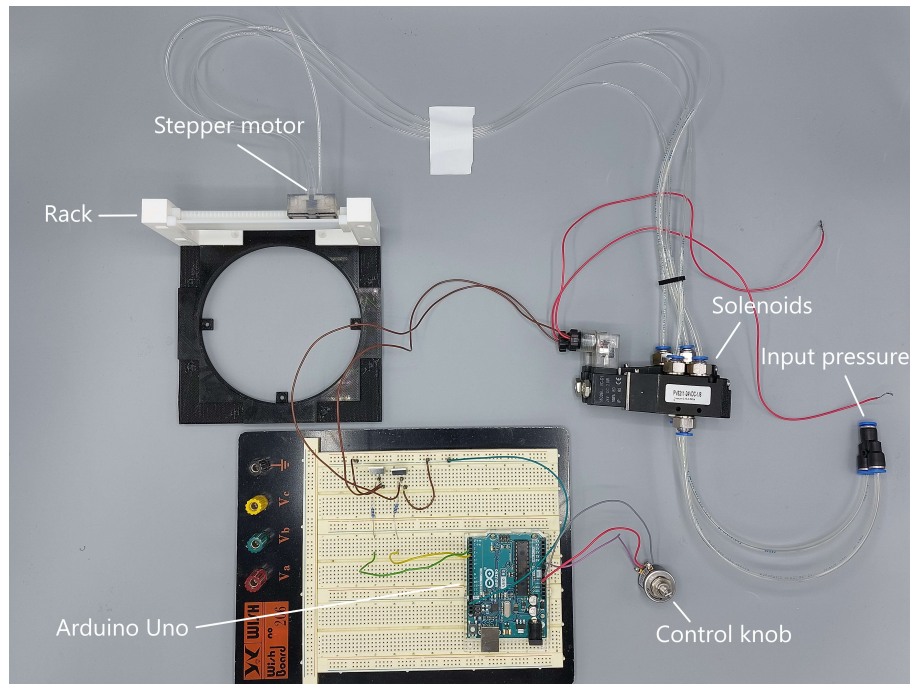


Figure 5.4: Motor setup used to determine the accuracy of the encoder. A pneumatic stepper motor was controlled using an Arduino Uno. The power supply, pneumatic supply tube and USB connection to a PC have been omitted in this picture.

The pneumatic stepper motor was controlled using an Arduino Uno. For each measurement, the stepper motor was controlled to step anywhere between 1 mm and 40 mm. This distance was measured using calipers. Next, the algorithm was used to determine the travelled distance as measured by the sensor. The starting position was always in a position corresponding to zone 0 or zone 1 to align with the initial conditions of the algorithm. Because of the asymmetry of the sensor response, the motor was tracked going in a positive and negative direction. For each direction, 40 measurements were taken. To set suitable values for the four different thresholds, an initial measurement was done across the full range. The thresholds were manually selected from this calibration measurement.

The sensor response was recorded at 1800 Hz. The signal was filtered using a moving average filter across 200 measurements. The slope was calculated from the filtered signal and another moving average across 15 elements was applied on the slope. The motor was set to move at 16 Hz on a rack with a pitch of 2.5 mm.

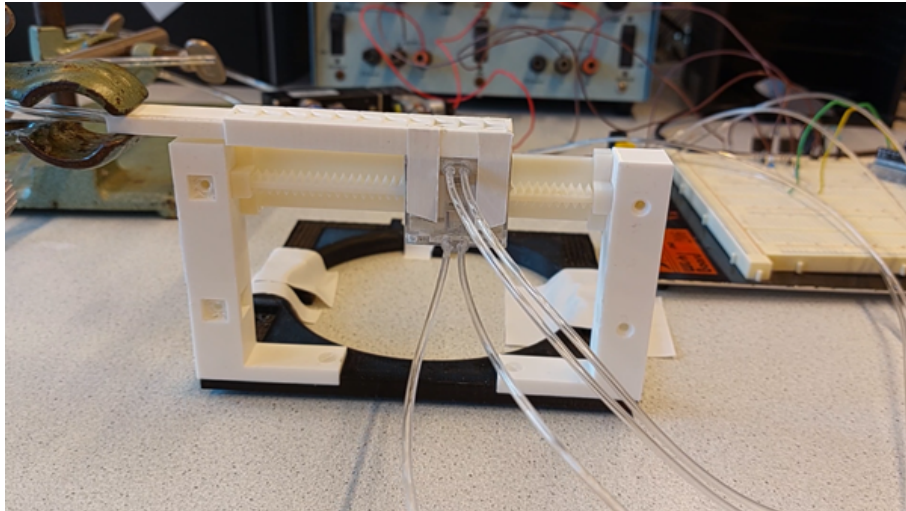


Figure 5.5: Encoder taped onto the pneumatic stepper motor.

5.2 Results

Figure 5.6a shows the results of the static measurement. The linearity between 0 mm and 5 mm is rather poor, so an additional line piece is added to the piecewise linear approximation.

Figure 5.6b shows the final error for each of the 80 measurements. The mean error is -0.86 mm. The threshold values were determined manually from a calibration measurement. The low threshold was 2.9 V, the middle threshold was 3.2 V and the high threshold was 3.7 V. The slope threshold was 3.5×10^{-3} V/sample.

For illustration, the full sensor response of the measurement with the largest error is included in figure 5.6c.

5.3 Discussion

Ideally, the static response would be linearised more, to have a clearer distinction between the zone 2 and the other zones. The geometry used is based on a characterisation performed on a larger scale. Redoing this linearisation on the scale that is used in the encoder (6 mm) can improve linearity and therefore also the ability to recognise zone 2. This would reduce the amount of pieces needed to model the response.

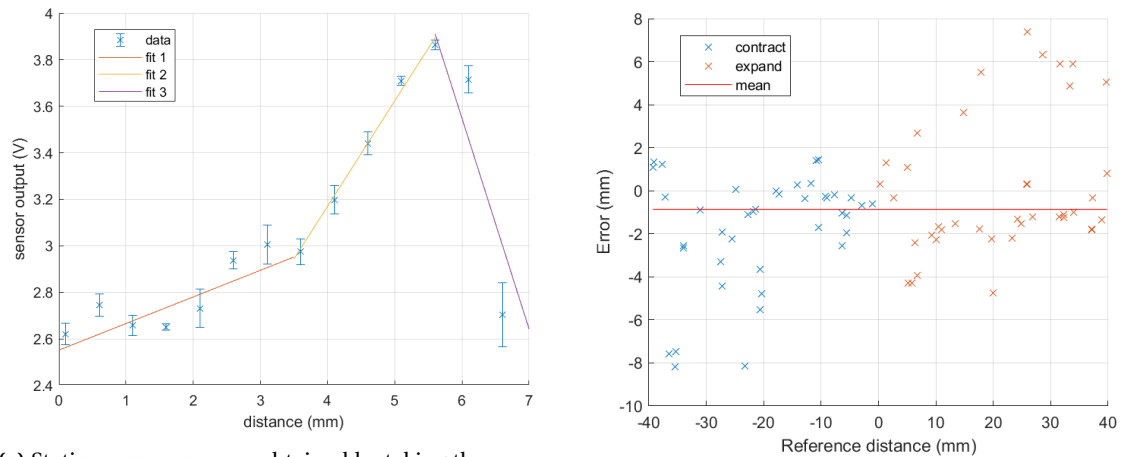
Additionally, it is notable that the modeled sensor response from figure 5.2 includes an upward trend after 6 mm that is not visible in the measured data. This is likely to an underestimation of leakage in the model. This is in part caused by the fact that the model is used to estimate the sensor response when the orifice is fully covered, even though this data is not included in the model itself. Since this modeled response is mainly used for designing the segment counting algorithm and it is not used for actual position estimation, the effects of the deviation from the model are limited.

The error distribution seems to spread for larger absolute reference distances. For negative references this spread is towards underestimation of the distance and for positive reference distances this spread is towards overestimation of the distances. A reason for this could be the difference in output signal per segment that can be seen in figure 5.6c. This offsets the signal with respect to the linear models used to estimate the position within a segment. For values near the high threshold en low threshold, this effect is smaller since the estimation within a segment is limited to the range of 0 mm to 7 mm.

Furthermore, the algorithm usually counts the right number of segments, since the error is mostly smaller than 7 mm. However, figure 5.6c is a counterexample. At 7 seconds, the sensor

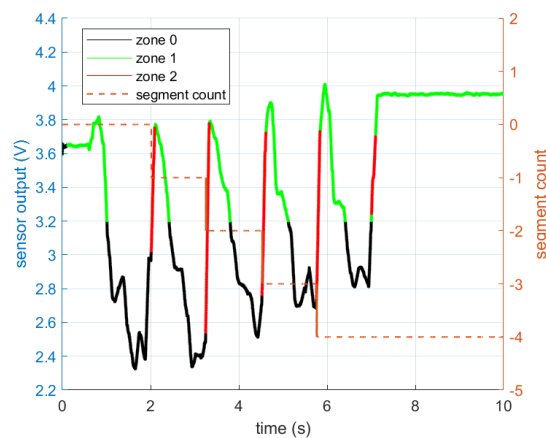
value passes the low threshold before surpassing the slope threshold, which leads to the algorithm missing a count. Better similarity between segments or a larger distinction between the slope in zone 2 and the other zones could both resolve this problem.

In general, there are many parameters that could be tuned to optimise this encoder. Longer encoder holes decrease sensitivity within a segment, but increase the contrast between zone 2 and the other zones. Also, methods could be investigated to decrease the difference between the segments. Alternatively, a piecewise linear approximation of the full range could also improve accuracy. Finally, the algorithm for segment counting is rather basic. More advanced algorithms, possibly aided by machine learning may be able to improve the accuracy of segment counting.



(a) Static sensor response obtained by taking the mean of three measurements across three different segments (9 measurements per data point in the plot). A piecewise linear approximation is also displayed. Error bars display CI95% of the mean.

(b) Errors measured for various stepper motor displacements. Both movements that expand (orange cross) and contract (blue cross) the sensor head have been measured. The mean error of -0.86 mm is displayed as well.



(c) On the left axis, the measured signal of the measurement with the largest absolute error is displayed. The reference distance was -35.5 mm and the measured distance was -27.3 mm. The zones as recognised by the algorithm are indicated. On the right axis, the segment count as recognised by the algorithm is displayed.

Figure 5.6: Results from static and dynamic measurements on the pneumatic encoder.

6 Conclusion

6.1 Conclusion

In conclusion, this project describes a method to design and fabricate a linear pneumatic position sensor. Its intended application is providing feedback to robotic systems in MR-environments. The research questions are answered below and a reflection on the project goal is provided.

Which requirements does the MR-environment impose on the sensor design?

Robotics in an MR-environment are inherently different from regular robotics because the use of conductive materials should be avoided or at least be limited to a small amount to protect the functioning of the robot and guarantee the safety of the operators or patients that come near the robot. This requires an alternate approach to sensing. The sensor designed in this project therefore only requires standard pneumatic tubing made out of polyurethane and a 3D-printed sensor head made out of PLA to be inside the MRI-room. Pneumatic tubing connects the sensor head to the rest of the sensor that is located outside of the MRI-room.

Which requirements does the robotic system impose on the sensor design?

The application that is considered in this design (IRE) requires a positional accuracy of about 1-2 mm (Glossop, 2012). A fast response time is preferred, though the intended (medical) applications do not strictly need to move quickly. It should be noted that even though a particular application was envisioned, the design of the position sensor kept general on purpose. The absolute maximum error observed on the realised sensor was 16% of the total range. This makes the sensor not yet usable for robotic applications.

How can translational motion be transduced into a differential pressure signal?

The design used in this project is based on the idea that airflow through a pneumatic tube can be modulated by changing the size of an orifice that connects the pressurised air to the ambient air. An initial prototype was 3D printed using PLA through an FDM process. This prototype was used to linearise the sensor output as a function of the measured displacement. An empirical process of prototyping and measuring the characteristics of each prototype enabled improvements to the sensor.

Goal *To design a pneumatic position sensor for robotic applications in an MR-environment.*

A pneumatic position sensor had been designed with a range of 45 mm. The output of the sensor is between 2.6 V and 4.9 V. The maximally observed standard deviation on the output voltage upon repeated measurements is 0.09 V. The maximally measured linearity error is 10.6% of the total range. The accuracy is characterised by an absolute mean error of 0.31 mm (0.7% of the full range) and an absolute maximum error observed is 7.2 mm (16.0% of the full range). Additionally, a pneumatic encoder was created with a mean error of 0.81 mm (2.0% of the tested range) and an absolute maximum error of 8.2 mm (20.5% of the tested range).

The final pneumatic sensor and encoder do not meet all the requirements for providing adequate feedback to a robotic system. Major obstructions to achieving these requirements include the difficulty to fabricate small, parts precisely and accurately with the tools available. The transferability of the sensor design to different manufacturing systems and materials is low, which made the scaling of the sensor difficult. Though these issues are resolvable through

extensive effort to calibrate the fabrication process on a particular machine, the strong dependence on accurate fabrication can be considered a flaw in the current design.

6.2 Future work

Improvements in the field of pneumatic position sensing can be achieved in a multitude of ways. As for improving the current sensor design, the same process as followed in this project can be followed but using a high quality printer from the start to obtain more consistent results across the calibration process. Possibly, a study into the leakage in the sensor head due to air flow between the inner and outer tube can give additional insights into the parameters that need to be controlled to make the design transferable between different manufacturing machines. Also, better use could be made of the output of the differential pressure sensor, by designing circuitry to remove the offset signal and amplify the remainder. For instance, this could be done using a simple inverting operational amplifier circuit. A sensitivity increase would be the result. Additionally, research could be done into reducing the sliding friction in the sensor head as to reduce the load these sensors pose on the pneumatics. Additionally, the results of this project could be used to design rotary position sensors to accommodate the sensing of different joint configurations.

To mitigate some of the issues with the sensor design, the pneumatic encoder was created. Especially scaling of the sensor while limiting the loss of sensitivity should be easier with the encoder. However, time constraints did not allow the encoder design to be iterated, which still leaves a lot of room for improvement. Optimisation possibilities of segment length, estimation of position within a segment and segment counting algorithms give the encoder design a lot of potential for improvement.

Another option is to design a pneumatic position sensor based on laminar flow. This approach would allow for better analytical modelling and it would also reduce power usage and noise.

To the best of the author's knowledge, there are currently no pneumatic position sensors in use for position feedback in medical robotics. This project has explored the first steps in how such a sensor could be realised and what challenges come along with it. Although the final product does not yet fulfill the requirements to provide position feedback, from this project it can be concluded that there is potential for pneumatics to be used in position sensing.

A Pictures of sensor heads

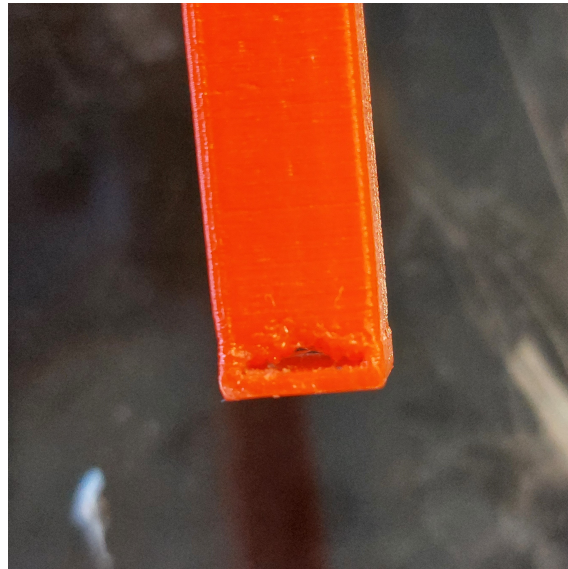


Figure A.1: Slit in inner tube of prototype 1 printed using the Ultimaker 2

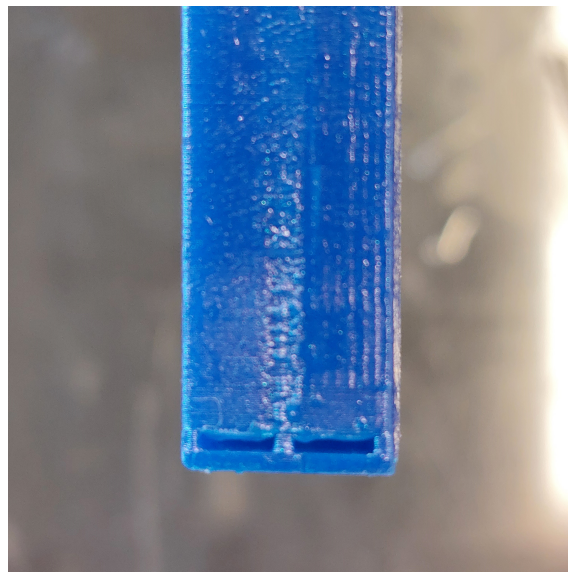


Figure A.2: Slit in inner tube of prototype 3 printed out of PLA using the Ultimaker 5S



Figure A.3: Slit in inner tube of prototype 4 printed out of VeroWhite using the Connex3

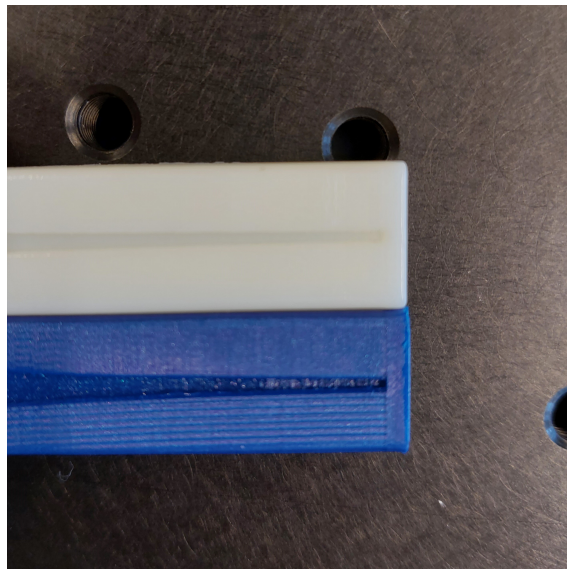


Figure A.4: Comparison of the encoder hole on the outer tube of prototype 3 (Blue PLA) and 4 (VeroWhite). The white prototype has a visibly narrower gap at the right edge of the encoder hole even though the gaps should be equally wide at that point.

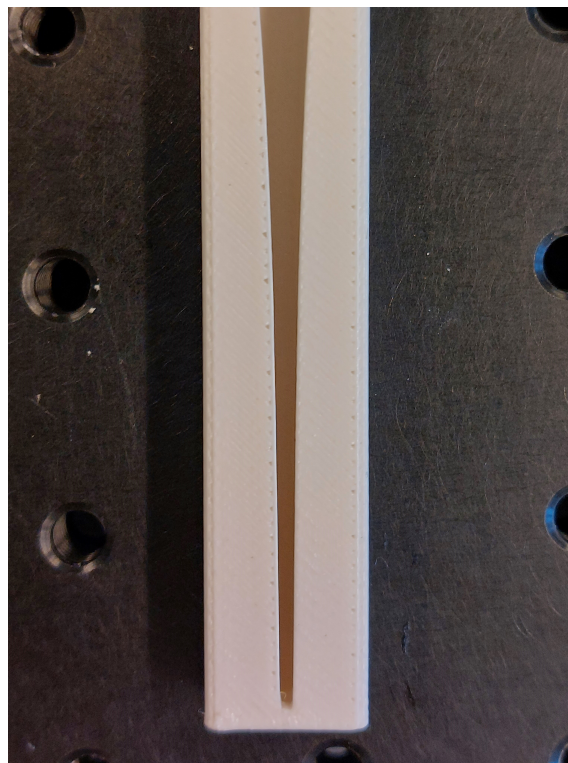


Figure A.5: Outer tube of prototype 5 as produced by the Fortus using ABS. Black dots close to the edge of the encoder hole are pores.

B Multiple Regression

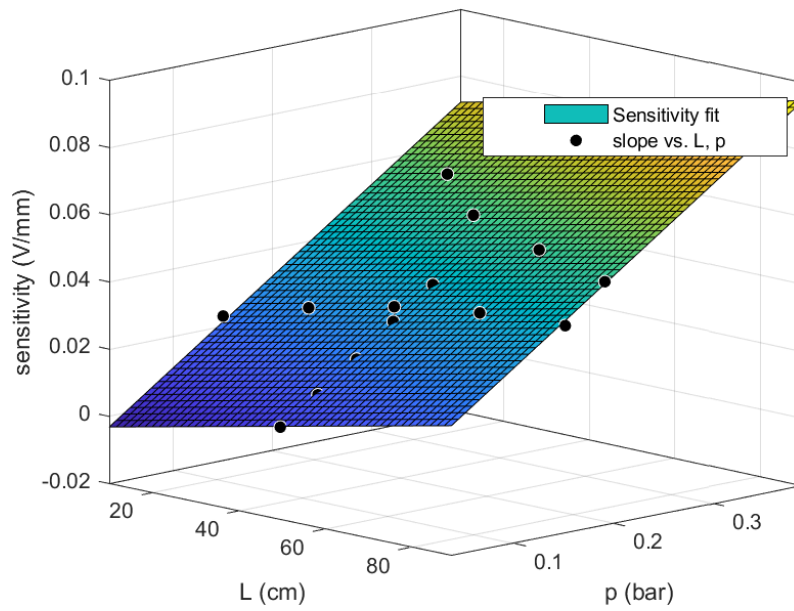


Figure B.1: Linear fit predicting the sensitivity from the input pressure and length of the measuring tube

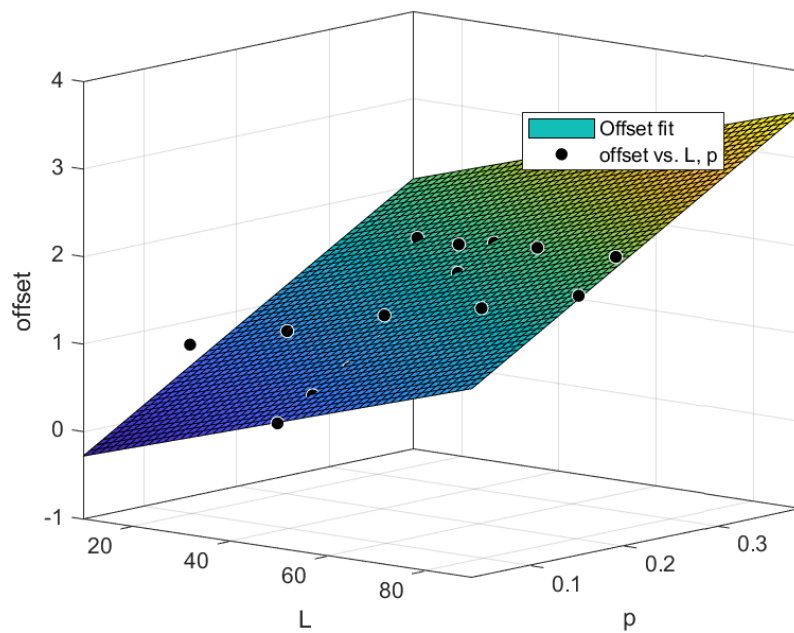


Figure B.2: Linear fit predicting the offset from the input pressure and length of the measuring tube

Bibliography

- Elhawary, H., A. Zivanovic, M. Rea, B. L. Davies, C. Besant, D. McRobbie, N. M. Desouza, I. Young and M. U. Lampérth (2008), A modular approach to MRI-compatible robotics, **vol. 27**, no.3, pp. 35–41, ISSN 07395175, doi:10.1109/EMB.2007.910260.
- Franco, E., D. Brujic, M. Rea, W. M. Gedroyc and M. Ristic (2016), **vol. 21**, no.2, doi:10.1109/TMECH.2015.2476556.
- Gassert, R., R. Moser, E. Burdet and H. Bleuler (2006), MRI/fMRI-compatible robotic system with force feedback for interaction with human motion, **vol. 11**, no.2, pp. 216–224, ISSN 10834435, doi:10.1109/TMECH.2006.871897.
- Georgantopoulou, C. G. and G. A. Georgantopoulos (2018), 5.6 Turbulent Flow in Pipes, in *Fluid Mechanics in Channel, Pipe and Aerodynamic Design Geometries 1*, John Wiley & Sons, ISBN 978-1-78630-139-0.
- Glossop, N. (2012), Localization and tracking technologies for medical robotics, *Woodhead Publishing Series in Biomaterials*, pp. 41–58.
- Groenhuis, V., F. Siepel and S. Stramigioli (2018), Dual-Speed MR Safe Pneumatic Stepper Motors, in *Robotics: Science and Systems 2018, RSS 2018*, Robotics: Science and Systems Foundation, doi:10.15607/RSS.2018.XIV.030.
- Groenhuis, V., F. J. Siepel and S. Stramigioli (2020), Sunram 5: A Magnetic Resonance-Safe Robotic System for Breast Biopsy, Driven by Pneumatic Stepper Motors, doi:10.1016/B978-0-12-814245-5.00022-0.
- Kwoh, Y. S., J. Hou, E. A. Jonckheere and S. Hayati (1988), A Robot with Improved Absolute Positioning Accuracy for CT Guided Stereotactic Brain Surgery, **vol. 35**, no.2, pp. 153–160, ISSN 15582531, doi:10.1109/10.1354.
- Liu, W., Z. Yang, S. Jiang, D. Feng and D. Zhang (2020), Design and implementation of a new cable-driven robot for MRI-guided breast biopsy, **vol. 16**, no.2, p. e2063, ISSN 1478-596X, doi:10.1002/RCS.2063.
- Navarro-Alarcon, D., S. Singh, T. Zhang, H. L. Chung, K. W. Ng, M. K. Chow and Y. Liu (2017), Developing a Compact Robotic Needle Driver for MRI-Guided Breast Biopsy in Tight Environments, **vol. 2**, no.3, pp. 1648–1655, ISSN 23773766, doi:10.1109/LRA.2017.2678542.
- Senturk, Y. M. and V. Patoglu (2017), MRI-VisAct: a Bowden-cable-driven MRI-compatible series viscoelastic actuator, **vol. 40**, no.8, pp. 2440–2453, ISSN 14770369, doi:10.1177/0142331217730429.
- Shametaj, P. (2021), Positioning and orientation control of a needle-Insertion MRI compatible medical robot based on ROS using visual feedback - University of Twente Student Thesis. <https://essay.utwente.nl/86070/>
- Siepel, F. J., B. Maris, M. K. Welleweerd, V. Groenhuis, P. Fiorini and S. Stramigioli (2021), Needle and Biopsy Robots: a Review, **vol. 2**, no.1, pp. 73–84, ISSN 2662-4087, doi:10.1007/S43154-020-00042-1.
- Taffoni, F., D. Formica, P. Saccomandi, G. Di Pino and E. Schena (2013), Optical fiber-based MR-compatible sensors for medical applications: an overview, **vol. 13**, no.10, pp. 14105–14120, ISSN 1424-8220, doi:10.3390/S131014105.
- Unger, M., J. Berger and A. Melzer (2021), Robot-Assisted Image-Guided Interventions, *Frontiers in Robotics and AI*, **vol. 8**, p. 221, ISSN 22969144, doi:10.3389/FROBT.2021.664622/BIBTEX.
- U.S. Department of Health and Human Services (2021), Testing and Labeling Medical Devices for Safety in the Magnetic Resonance (MR) Environment Guidance for Industry and Food

and Drug Administration Staff This document supersedes Establishing Safety and Compatibility of Passive Implants in the Magnetic Resonance (MR) Environment.

<https://www.regulations.gov>.

Xinran, Z., D. Haiyan, L. Mingyue and Z. Yongde (2021), Breast intervention surgery robot under image navigation: A review:, **vol. 13**, no.6, pp. 1–17, ISSN 16878140, doi:10.1177/16878140211028113.

Yang, B., S. Roys, U. X. Tan, M. Philip, H. Richard, R. P. Gullapalli and J. P. Desai (2014), Design, Development, and Evaluation of a Master-Slave Surgical System for Breast Biopsy under Continuous MRI, **vol. 33**, no.4, p. 616, ISSN 17413176, doi:10.1177/0278364913500365.